Definition of geochemical domains in a chromite mine, Bushveld Complex, South Africa

Kai Bachmann, Peter Menzel, Raimon Tolosana-Delgado, Jens Gutzmer
Helmholtz Institute Freiberg for Resource Technology

Abstract. The Lower and Middle Group chromitites of the Bushveld Complex are the source of a very large portion of the global chrome supply. Yet, the effectiveness of chromite beneficiation circuits is highly sensitive to mineralogical and textural variations in feed composition. The use of geochemical proxies, based on data acquired routinely during the exploration and mining process may provide a cost- and time-efficient alternative to more time-consuming and expensive mineralogical analyses. Such an approach is presented in this study, which focuses on the LG-6, LG-6A, MG-1 and MG-2 chromitite seams at the Thaba mine located on the western limb of the Bushveld Complex. According to a sound statistical assessment, the chromitites of the Thaba mine area can be subdivided into three distinct domains, domains that constitute the suitable fundamental for a geometallurgical model. Accordingly, a least altered (orthomagmatic) domain is distinguished from a supergene altered domain and a domain affected by widespread hydrothermal alteration. The latter domain occurs below the depth of modern weathering, but in obvious proximity to faults and around a prominent dunite pipe. The orthomagmatic domain is represented by ores least affected by post-magmatic alteration processes. This domain occupies the centre of fault blocks below the extent of modern weathering.

1 Introduction

Besides vast resources of chromium, the Critical Zone of the Rustenburg Layered Suite (RLS) in the Bushveld Complex represents the largest global resource of platinum-group elements (PGE) as well as significant resources of Ni and Cu (e.g., Maier et al. 2013). A significant portion of the geological chromium and PGE resources is hosted together with chromite in a series of chromitite layers, subdivided according to their stratigraphic position in the Critical Zone into the Lower, Middle and Upper Groups (LG, MG, UG; Cousins and Feringa 1964). In general, LG and MG layers have a higher chromium content (>46% Cr_2O_3 in the LGs) and are mined for chromite, compared to the UGs (<42% Cr_2O_3). This trend is accompanied by a decrease of their Cr/Fe ratio from >1.8 to <1.3 (e.g. Viljoen 2016).

The bulk of the LG and MG chromitites extracted in the Bushveld Complex have an orthomagmatic mineral assemblage dominated by chromite (>50 wt% to 95 wt%) and associated gangue silicates, predominantly orthopyroxene and plagioclase (Kinnaird et al. 2002). This orthomagmatic assemblage has been noted to be affected by surficial weathering (down to 50 m; e.g. Junge et al. 2015) and hydrothermal alteration (e.g. Voordouw et al. 2010). Becker et al. (2014) report an enrichment of alteration silicates (amphibole, chlorite, serpentine, talc) and Fe-oxides/hydroxides, as well as depletion in BMS (base metal and Fe sulfides) as a result of weathering.

This change in gangue mineralogy will have significant impact on the chromite beneficiation process, for both the grinding and the separation circuits. A shift in mineralogy towards alteration silicate-rich chromitite compositions will result in a higher amount of fines, which will reduce the performance of the subsequent unit operations (Murthy et al. 2011 and references therein). Equally important will be the effect of alteration on density separation techniques, such as spirals; an increase in fine particle sizes (<100 µm) will negatively impact the recovery during gravity separation – a significant amount of chromite will be lost to the tailings (Gence 1999). Murthy et al. (2011) reported that up to 25 % of the mineral value originally contained in the chromite ore is lost as slimes during beneficiation.

The scope of this study is to investigate the bulk geochemistry of a large number of drill cores of four chromitite seams of the Thaba mine (operated by Cronimet Chrome Mining SA (Pty) Ltd), to discuss the variability within and between the distinct seams and to separate the mine lease area into distinct geochemical clusters. These clusters are then related to the geological architecture in the mine lease area. The results are combined with knowledge concerning the quantitative mineralogical composition of selected samples achieved in Bachmann et al. (2018). This leads to the definition of domains that can be clearly distinguished based on their mineralogical, geochemical and geological characteristics. It is expected that these can also be used as a solid foundation of a geometallurgical model for the deposit.

2 Data and Methodology

To understand the geological architecture, a geological model of the Thaba mine focusing on four target chromitite layers and containing 771 chemical assays (LG-6: 339; LG-6A: 242; MG-1: 57; MG-2: 133) was developed. The geological model is based on 270 drill core logs containing collar location, depth and survey and geological information. The model is displayed in Figure 1 (see Bachmann et al, 2019, for reference). The data set provided by the mine owner, which comprises data for Cr_2O_3, FeO, Al_2O_3, MgO, SiO_2, CaO and P, was evaluated. Details on the quality of the data set, performed corrections for sample batches and analytical methods can be found in Bachmann et al. (2019).

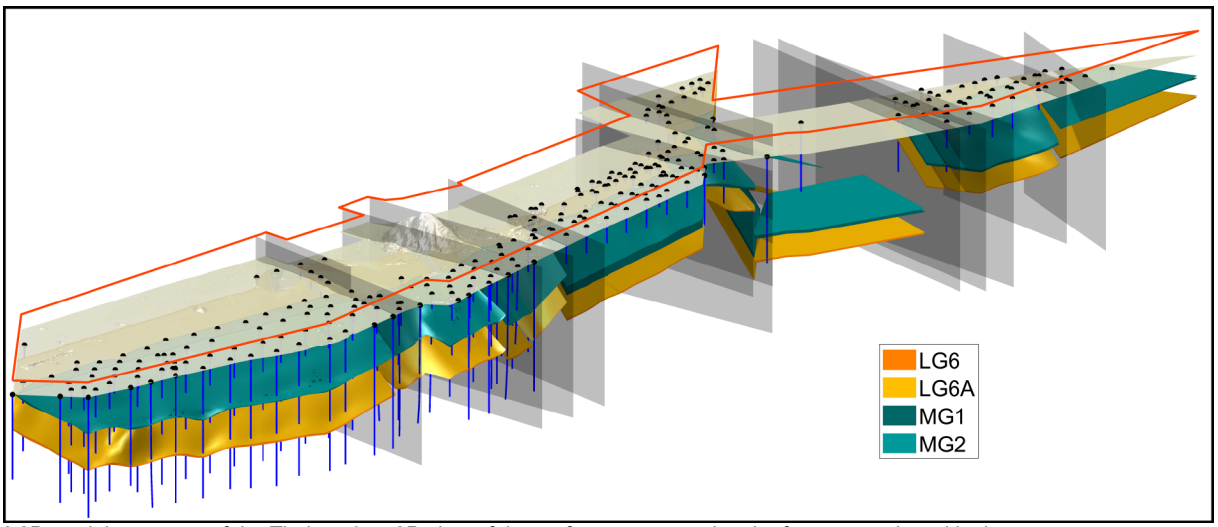

Figure 1 3D model geometry of the Thaba mine. 3D view of the surfaces representing the four target chromitite layers.

3 Results and Discussion

Cluster analysis was performed separately for LGs and MGs, respectively. Figure 2A displays a distinct separation into four clusters for geochemical data of the LG-6 and LG-6A. While cluster 1 represents samples high in Cr_2O_3 and low in CaO/SiO_2, cluster 2 shows a slight but systematic shift to SiO_2 and CaO enriched compositions. Cluster 3 is dominated by outliers with high CaO and/or SiO_2 contents, while Cr_2O_3 shows, in general, lower concentrations. The "supergene" cluster represents all drill core intersections classified as cluster 2 and are within the first 50 m below surface. Whether the drill core intersections of this cluster were already altered prior to being exposed to weathering cannot be determined. Additionally, the results display systematic trends that are independent of the actual chromitite layer considered.

Figure 2B shows the results of the corresponding cluster analysis for MG-1 and MG-2. Note that PC3 is shown on the y-axis, displaying similar loadings as PC2 in Figure 2A. On the other hand, PC2 of the MGs corresponds to PC3 of Figure 2B (as well as PC3 of the LG's), showing strong loadings on phosphorous. Hence, due to limited data points, cluster discrimination for the MG chromitites is not as significant as for the LGs, but appears more "noisy". Nevertheless, overall trends are similar to the LGs, representing a shift towards SiO_2/CaO richer compositions from cluster 1 through cluster 2 to the "Supergene" cluster. As shown in Figure 2A, cluster 3 predominantly represents outliers with either high phosphorous or CaO contents. Similar to the LG-6/LG-6A, trends do not distinguish MG-1 from MG-2.

3.1 Linking geochemistry with mineralogy

The mineralogy of chromitite seams of the LGs and MGs is well known and has been previously described in detail (e.g. Naldrett et al. 2012 and references therein), as well as for the Thaba Mine lease area (Bachmann et al. 2018).

Firstly, Cr_2O_3 occurs almost exclusively in chromite and mineral compositions of chromite show only slight variation, thus the assumption to link increasing Cr_2O_3 contents with increasing chromite concentrations is valid. Silicate minerals in primary orthomagmatic chromitites are orthopyroxene, minor clinopyroxene, olivine, feldspar (mainly plagioclase) and dark micas with biotitic compositions. This rock-forming mineralogy is well reflected by the available chemical assays, with minor exceptions, such as V, Ti, and Mn, usually accounting for not more than 1-2 wt% in total. Furthermore, iron was only measured as FeO, but in reality, iron is present as both FeO and Fe_2O_3, which again will account for another few wt% in total. It can be concluded that the chemical assays contained in the database should account for >97 wt% of the total chemical composition of a typical orthomagmatic chromitite sample. Yet, there is a significant number of analyses with totals below 95 wt%. Analyses with low totals display a significant positive correlation with increasing SiO_2 and CaO concentrations, and are also marked by an abundance of alteration minerals, such as chlorite, talc, serpentine and amphibole (Bachmann et al., 2018). Furthermore, significant amounts of carbonate minerals such as calcite and dolomite are present in some samples. Hey (1999) documented that clay minerals (e.g. smectites) are common in chromitites affected by supergene alteration. These alteration minerals incorporate certain amounts of volatiles (water, carbonate) – constituents not included in the assay data set. Therefore, low totals are attributed to high abundances of alteration minerals. Alteration will, however, also change the relative abundance of certain elements within the data set. Due to the high resistance of chromite to alteration, the absolute amount of chromite will remain rather consistent, while the gangue mineral assemblage can change dramatically. An increase in volume of the seams, for example, will decrease the relative amount of chromite, hence, the Cr_2O_3 concentration decreases. All these parameters can be used as a proxy to detect alteration.

.

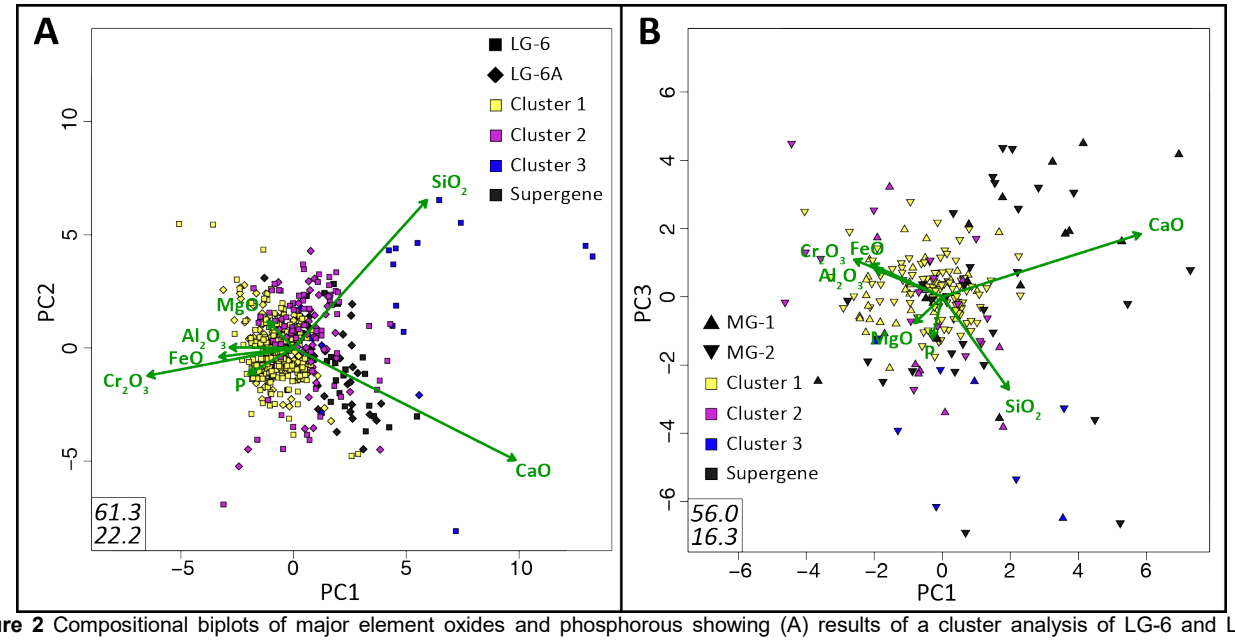

Figure 2 Compositional biplots of major element oxides and phosphorous showing (A) results of a cluster analysis of LG-6 and LG-6A chromitites (first (x-axis) vs. second (y-axis) principal components; PC) and (B) of MG-1 and MG-2 chromitites (first (x-axis) vs. third (y-axis) PC). The compositional contrast between LG-6/ LG-6A and MG-1/ MG-2, respectively, was minimized by matching the means of each seam.

3.2 From chemical clusters to geochemical domains

The integration of geochemical clusters into the geological 3D model allows recognition of the inherent relations between geochemistry and geological architecture. As shown in Figure 3, clusters form distinct geochemical domains. General trends are similar for both the LG-6 and LG-6A. While cluster 1 can be allocated to the southern part of the deposit, cluster 2 and the "supergene" cluster are, in general, located in the north of the mine lease area. Cluster 3 comprises outliers and can hardly be translated as a distinct geochemical domain, but points towards chemical anomalies within the deposit. For the LGs, cluster 1 shows homogeneous elemental distribution including high Cr_2O_3, Al_2O_3 and FeO concentrations, while SiO_2 and CaO contents are low. The spatial distribution of this most pristine cluster seems to be connected to the distribution of troctolite. Troctolite is believed to cause metasomatization and/or replacement of orthomagmatic mineral assemblages (Voordouw et al. 2010) inducing increasing CaO and Al_2O_3 (plagioclase) and MgO (olivine) concentrations. However, we cannot observe such systematic changes in mineralogy in the majority of samples within cluster 1. Nevertheless, in the rare cases, when troctolites are emplaced in direct contact with the chromitite seams, they cause dramatic changes in the chemistry. Cluster 2 comprises chromitite samples affected by different types of alteration, with generally lower grades in Cr_2O_3 and increased SiO_2 and/or CaO. On the one hand, these alteration processes are associated with the Middellaagte IRUP (iron-rich ultramafic pegmatite; e.g. Scoon and Mitchell 1994) and form a halo of metasomatization/hydrothermal alteration. On the other hand, alteration is related to serpentinization within and immediately around fault zones in the central portion of the mine lease area.

The "supergene" cluster forms a domain of supergene altered/oxidized ore and displays even lower Cr_2O_3 grades than the pristine and altered domains, while SiO_2, CaO and FeO concentrations increase. As defined above and in accordance to literature (Junge et al. 2015), supergene alteration is restricted to intersections <50 m below surface. It appears reasonable to expect a rapid gradational contact between the supergene and pristine ore zones, although this remains to be tested. This notion is supported by results of the present study, because not all intersections <50 m are classified to the "supergene" cluster. Nevertheless, to define a transition zone between oxidized and pristine ores, the spatial resolution of the data set would have to be significantly higher. Similar to the LGs, integration into the geological geometry of the defined chemical clusters was performed for the MG chromitites. Due to the limited amount of data for the MG-1 (only ~50 intersections), defining precise domains using chemical clusters was challenging. Nevertheless, it can be stated that the data sets of MG-1 and MG-2 show a similar behavior; it appears thus reasonable to assume that both seams also have similar domains.

4 Conclusions

This case study illustrates how the combination of geochemical and geological data, complemented by tailored statistical evaluation, can provide a sound foundation for geometallurgical domaining and modelling. According to our assessment, three distinct geochemical domains are developed within the Thaba chromitite deposit. Firstly, the supergene altered domain is clearly differentiated from domains that are below the extent of modern day weathering. The chromitites below

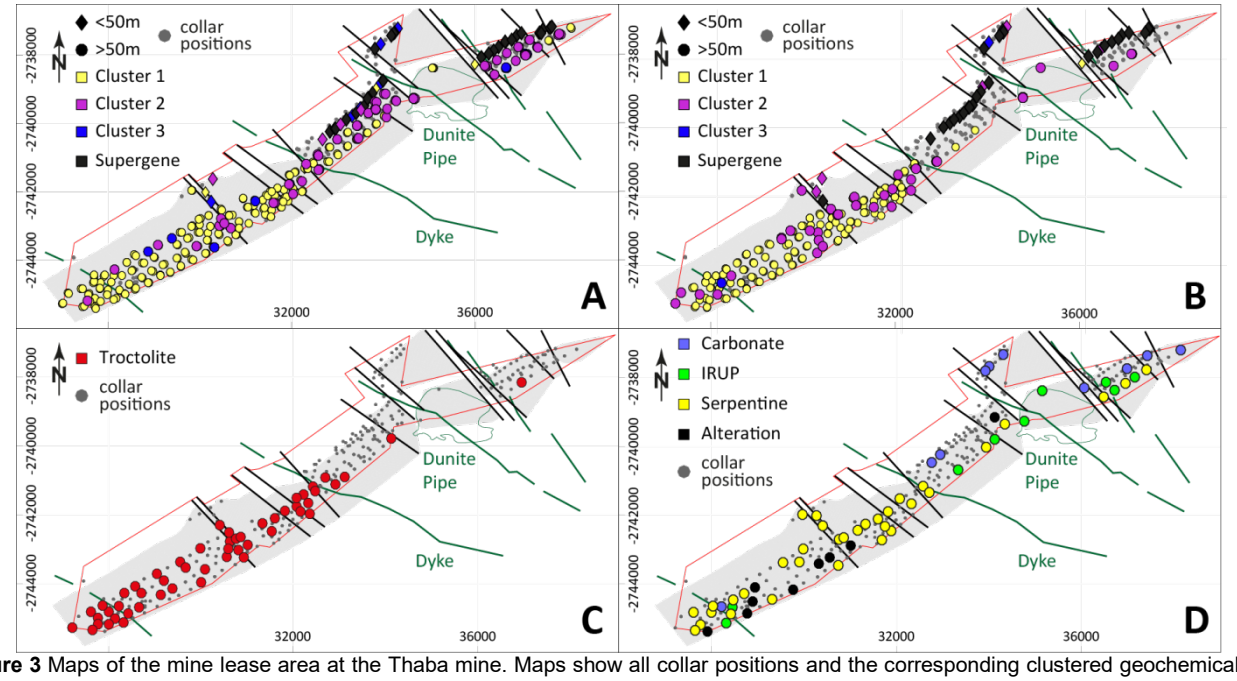

Figure 3 Maps of the mine lease area at the Thaba mine. Maps show all collar positions and the corresponding clustered geochemical data (according to Figure 10) of (A) the LG-6 and (B) the LG-6A. Maps displaying all alteration markers in close vincinity (150 m vertical and horizontal) to the seam intersections are shown in (C) for troctolite and (D) for all other alteration markers. Please note, all drill core intersections <50 m depth are displayed as diamonds; drill core intersections >50 m depth are shown as circles.

the depth of weathering can be further subdivided into a pristine domain with a predominantly orthomagmatic composition – and a domain affected by hydrothermal alteration processes. The latter domain is developed – sensibly – along fault structures and around the Middellaagte IRUP. These domains are crucial to design a sensible and tailored beneficiation process for chromitite ores, where the pristine domain will show superior processing characteristics for chromite beneficiation.

Acknowledgements

This is a contribution of the German/South African R&D project AMREP funded by the German Federal Ministry of Education and Research (BMBF; grant number BMBF 033R119E). We thank the Cronimet Mining Group for providing access to their core shed and drill core intersections from the Thaba mine and for the contribution of additional analytical data as well as information on the local geology and beneficiation.

References

Becker M, Wiese J, Ramonotsi M (2014) Investigation into the mineralogy and flotation performance of oxidised PGM ore. Minerals Engineering 65:24–32.

Bachmann K, Osbahr I, Tolosana-Delgado R, Chetty D, Gutzmer J (2018) Variation in platinum group mineral and base metal sulfide assemblages in the Lower Group chromitites of the western Bushveld Complex, South Africa. Can Min, https://doi.org/10.3749/canmin.1700094.

Bachmann K, Menzel P, Tolosana-Delgado R, Schmidt C, Hill M, Gutzmer J (2019a) The use of assay data as a foundation for a geometallurgical model – the case of the Thaba Chromite Mine, South Africa. Journal of Geochemical Exploration. doi.org/10.1016/j.gexplo.2019.01.008

Cousins CA, Feringa G (1964) The chromite deposits of the Western belt of the Bushveld Complex. In: Haughton SH (ed) The geology of some ore deposits in Southern Africa, Johannesburg. Geological Society of South Africa 2:183–202.

Gence N (1999) Beneficiation of elazig-kefdag chromite by multi-gravity separator, Tr. Journal of Engineering and Environmental Sciences 23:473–475.

Hey PV (1999) The effects of weathering on the UG2 chromitite reef of the Bushveld Complex, with special reference to the platinum-group minerals. South Afr J Geol 102:251–260.

Junge M, Oberthür T, Kraemer D, Melcher F (2015) Distribution of platinum-group elements in pristine and near-surface ores from the Platreef, northern Bushveld Complex, South Africa. In: André-Mayer AS, Cathelineau M, Muches P, Pirad E, Sindern S (Editors). 13th Biennial SGA Meeting, 955–958.

Kinnaird JA, Kruger FJ, Nex PAM, Cawthorn RG (2002) Chromitite formation—a key to understanding processes of platinum enrichment. Applied Earth Science 111(1):23–35.

Maier WD, Barnes S-J, Groves DI (2013) The Bushveld Complex, South Africa: formation of platinum–palladium, chrome- and vanadium-rich layers via hydrodynamic sorting of a mobilized cumulate slurry in a large, relatively slowly cooling, subsiding magma chamber. Mineral Deposita 48:1–56.

Murthy YR, Tripathy SK, Kumar CR (2011) Chrome ore beneficiation challenges & opportunities–a review. Minerals Engineering 24(5):375–380.

Naldrett AJ, Kinnaird J, Wilson A, Yudovskaya M, McQuade S, Chunnett G, Stanley C (2009) Chromite composition and PGE content of Bushveld chromitites: part 1—the lower and middle groups. Trans Inst Min Metall B118:131–161.

Naldrett AJ, Wilson A, Kinnaird J, Yudovskaya M, Chunnett G (2012) The origin of chromites and related PGE mineralization in the Bushveld Complex: new mineralogical and petrological constraints. Mineralium Deposita 47:209–232.

Scoon RN, Mitchell AA (1994) Discordant iron-rich ultramafic pegmatites in the Bushveld Complex and their relationship to iron-rich intercumulus and residual liquids. Journal of Petrology 35(4):881–917.

Viljoen, M (2016) The Bushveld Complex. Episodes 39:239–268.

Voordouw RJ, Gutzmer J, Beukes, NJ (2010) Zoning of platinum group mineral assemblages in the UG2 chromitite determined through in situ SEM-EDS-based image analysis. Mineralium Deposita 45:147–159.

Key ore textures influencing separation behaviour of ores

Kate Tungpalan
W.H. Bryan Mining and Geology Research Centre, Sustainable Minerals Institute, The University of Queensland

Elaine Wightman
Julius Kruttschnitt Minerals Research Centre, Sustainable Minerals Institute, The University of Queensland

Cathy Evans
W.H. Bryan Mining and Geology Research Centre, Sustainable Minerals Institute, The University of Queensland

Abstract. Ore texture displays the fundamental ore properties that significantly influences processing behavior of ores. Of all texture characteristics, mineral grain size and mineral association are expected to have the greatest influence. These textural features can be used to predict the separation performance of ores. To obtain such micro-scale textural information is costly and time-consuming to be applicable to the entire deposit. Recent work has shown the contribution of vein-type mineralization in the separation behavior of ores. Since veins can be identified during core logging, it provides a cost-effective means of acquiring textural information relevant to mineral processing for the entire deposit. This can then improve geometallurgical characterization of separation performance, providing better understanding of separation variability within the deposit.

1 Introduction

The depletion of easily mined high-grade ore bodies has resulted in the industry being required to process lower grade, complex resources to meet the increasing demand for minerals (Albanese and McGagh 2011; Darling 2011; Randolph 2011). The trend is now towards mining and processing of low-grade and complex ores (Darling 2011; Yingling 1990). Such ores come with variable geological and mineralogical characteristics, and complex mineralogy and texture. Variable characteristics, and complex mineralogy and texture can result in large variations in metallurgical response and also causes challenges in processing (Carson 1995; Lorenzen and Barnard 2011; Yingling, 1990). Variability and the complex nature of ores are fundamental sources of risk that can often cause adverse economic impacts to mining operations (Dusci et al. 2007; Williams and Richardson 2004). Hence it is important to effectively characterize these types of ore bodies as early as possible in the project development process and assess their processing performance to enable the development of economic and optimized production.

2 Ore texture – key driver to mineral separation

A case study was performed on a copper porphyry deposit to assess its variability in separation performance. An integrated geometallurgical method was carried out to populate the exploration database with copper recoveries. The method applied a principal component analysis on the database to divide the deposit according to similar geological and mineralogical characteristics. Each group had a distinct set of dominant geological and mineralogical characteristics, which were then used as input terms to predict copper recovery. The group-based modelling provided an indication of the key geological and mineralogical characteristics influencing copper recovery that were not evident in the original exploration database. Two drill core samples belonging to one group, and another two samples from another group were selected to undergo physical tests. The drill cores were crushed into particles; a sub-sample underwent flotation test and another sub-sample underwent texture measurement through the Mineral Liberation Analyser (MLA) (Fandrich et al. 2007). Each drill core sample was treated and analysed individually. The predicted and measured recoveries, and measured ore texture are shown in Table 1 and Fig. 1.

Table 1. Predicted and measured recoveries and grade

	Predicted Recovery, %Cu	Measured Recovery, %Cu	Measured Concentrate Grade, %Cu
Sample A.1	79	90±1	2.63±0.08
Sample A.2	89	80±4	4.36±0.94
Sample B.1	80	90±1	3.84±0.08
Sample B.2	90	85±3	3.92±0.08

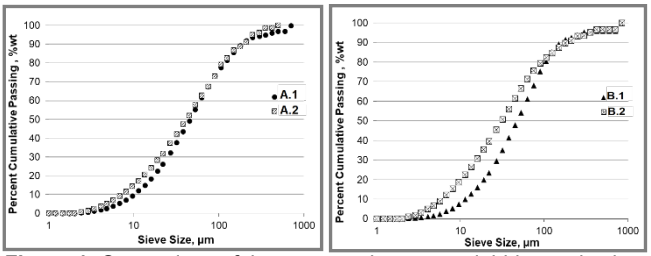

Figure 1. Comparison of the measured copper sulphides grain size distribution. (Left) Samples A.1 and A.2 have similar dominant geological and mineralogical characteristics, but A.1 exhibits slightly coarser copper sulphides grain size distribution and yielded higher measured copper recovery. (Right) Samples B.1 and B.2 also have similar dominant geological and mineralogical characteristics, but B.1 exhibits coarser copper sulphides grain size distribution and yielded higher measured copper recovery.

It was observed that there are discrepancies between experimental flotation recoveries and predicted recoveries. This indicated that the geological and

mineralogical data obtained from core logging which were used in the development of geometallurgical models for copper recovery were not capturing the underlying drivers for flotation response. However, the drill core samples yielded varying recoveries, which illustrates the usefulness of the integrated geometallurgical method in effective sampling of a variable deposit. Flotation is the most important and versatile separation technique that allowed the mining and processing of low-grade and complex ore bodies (Alexander et al. 2006). It is a complex process driven by several factors – from ore properties to operating parameters. It has been recognised that ore texture is representative of the fundamental ore properties that will determine the ease of mineral liberation and the subsequent mineral separation (Ferrara et al. 1989; Gaudin 1939; Jones 1987; King 1994; Petruk 2000). In metallurgy, the ore texture refers to the spatial arrangement, distribution, association, orientation, size and shape of the mineral grains that make up the ore (Barton 1991; Ferrara et al. 1989; Gaudin 1939; King, 1994; Preti et al. 1989). Of all texture characteristics, mineral grain size and mineral association are expected to have the greatest influence on processing behaviour (Evans 2010; Sutherland 2007; Tungpalan 2015). In the case study, it was found that the presence of coarser copper sulphide grains resulted in a higher degree of copper sulphides liberation as shown in Fig. 2, and higher copper recovery. The coarser mineral grains are easier to liberate compared to fine-grained minerals (Petruk 2000; Sutherland 1989). Consequently, the greater is the degree of liberation of the valuable minerals, it is highly likely that more valuable minerals will be recovered.

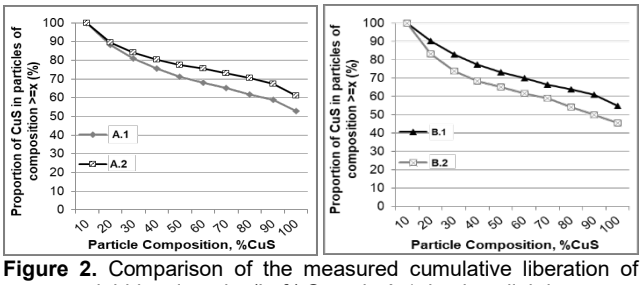

Figure 2. Comparison of the measured cumulative liberation of copper sulphide minerals. (Left) Sample A.1, having slightly coarser copper sulphides grain size distribution, yielded lower degree of liberation than A.2. This suggests that grain size is not the only key factor affecting the liberation of copper sulphides for these ores. (Right) Sample B.1, having coarser copper sulphides grain size distribution, yielded higher degree of liberation than B.2.

Mineral association also has an effect on the concentrate grade as well as the recovery. The case study showed that the ore where the copper sulphides are highly associated with sulphide gangue, particularly pyrite (Fig. 3), resulted in a higher copper recovery but lower concentrate grade. Since pyrite is a floatable mineral, particles (containing copper sulphides and pyrite) are more likely to float and hence have greater chances to be recovered. On the other hand, copper sulphides with higher degree of association with the non-floatable, non-sulphide gangue are less likely to be recovered, thus can lower the recovery.

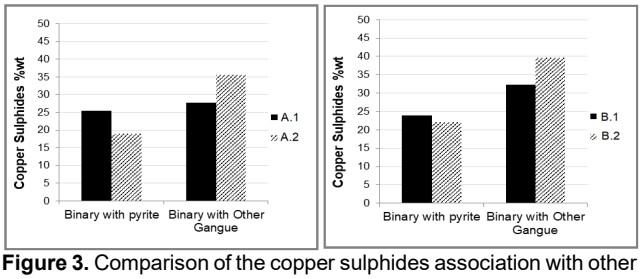

Figure 3. Comparison of the copper sulphides association with other minerals. (Left) The association between A.1 and pyrite is higher than between A.2 and pyrite; the association between A.1 and other gangue is lower than between A.2 and other gangue. The association of the copper sulphides with pyrite in sample A.1 could have caused its higher recovery despite having lower liberation of copper sulphides. This is also evident by the lower concentrate grade of sample A.1. (Right) The association between B.1 and pyrite is higher than between B.2 and pyrite; the association between B.1 and other gangue is lower than between B.2 and other gangue.

The results from analysis of the particles indicate that mineral grain size and mineral association are key textural drivers to separation behavior of ores. They provide valuable information for the grinding circuit and cleaner flotation. In particular, they could indicate the size to which the particles should be reduced to achieve optimum liberation. However, to obtain such detailed textural information is expensive and time-consuming to be practically applicable to the entire deposit. They are typically measured using high resolution measurement tools such as the MLA (Fandrich et al. 2007) and QEMSCAN (Sutherland and Gottlieb 1991). As a result, variability in separation performance within the deposit has not been fully understood. This points out the need to identify ore texture that are relevant to mineral separation at a larger scale i.e. drill core-scale. Recent works have shown the influence of mineralization styles in separation behaviour of ores, particularly of veins and disseminated grains (Tungpalan et al. 2017, 2018; Wightman et al. 2018). A drill core from the same copper porphyry deposit with evident veining structure was cut into semicircular slabs. Selected slabs were first analysed in the MLA to determine the extent of veining (Fig. 4). The slabs showed varied degree of sulphide veining from 11% to 22%. To investigate the influence of veining, the slabs were divided into two - those with ≤11% of sulphide veining were nominated as low and those with >11% were considered high. The slabs then underwent single impact breakage and analysed again in the MLA to measure the sulphides liberation. The measured sulphides liberation in the 600 micron particles (solid lines) and 300 micron particles (broken lines) are displayed in Fig. 5. It is evident that the presence of veins contribute to the ease of sulphides liberation. It was observed that the slabs with high extent of veining yielded higher degree of sulphides liberation. It was also observed that for the high veining, liberation of sulphides start to propagate even at 600 micron particles (indicated by the red line in Fig. 5). Whereas, in the low veining, sulphides start to liberate only at 300 microns.

Wightman et al. (2018) also examined the implications of disseminated grains on the liberation of gangue minerals. It was observed that the presence of disseminated grains, their grade and size distribution

have direct impact on the degree to which rejection of gangue minerals at coarse sizes is possible. The rejection of gangue at coarse particle size will also bring significant benefits in mineral processing.

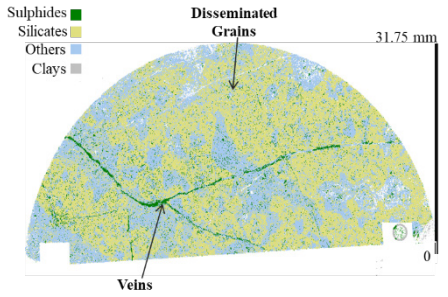

Figure 4. Slab image obtained from MLA showing veins and disseminated grains.

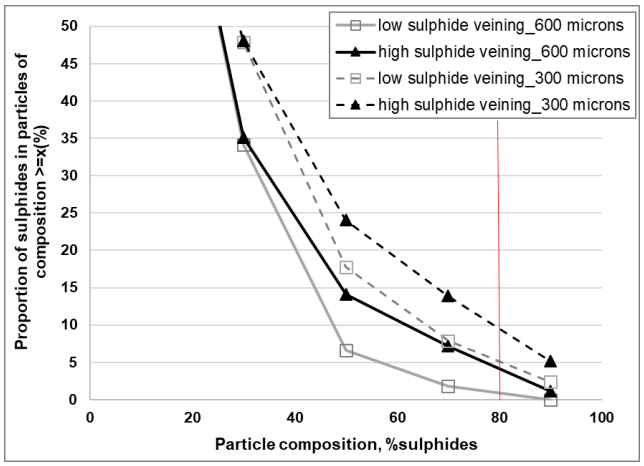

Figure 5. Cumulative liberation of sulphides measured from the slabs in the MLA. Greater veining contributed to an increased degree of sulphides liberation and contributed to propagation of liberated sulphides at coarser particle size.

More research work has to be done to gain better understanding of the role of veins and disseminated grains in separation behaviour of ores, particularly linking it with recovery. However, the work highlights the significance of vein-type mineralization in the ease of mineral liberation. The presence of veins contributes to an increased degree of liberation and also contributes to the propagation of liberated minerals at coarser particle sizes. Vein structures can be a proxy for separation performance, and is therefore a valuable tool for understanding potential mineral recoveries as early as the exploration phase. Since veins can be identified during drill hole logging without the use of expensive high resolution devices, it provides a cost-effective means of acquiring textural information relevant to processing for the entire deposit. The information from vein structures has potential benefits in improving geometallurgical characterization of separation performance, providing better understanding of the separation variability within the deposit. Logging of vein structures is therefore important and should include not only the type of vein but also the extent of veining.

3 Implications

It is apparent that the texture of the ore, particularly mineral grain size, mineral association and vein structures, have significant influence on copper sulphides liberation and copper recovery. This suggests the importance of describing texture to assess the separation performance of the deposit which then enables creation of strategies for optimized economic production. It is important to note that the scale at which detailed measurements of ore texture are undertaken is critical and needs to be carefully considered.

Acknowledgements

The authors would like to thank Professor Emmy Manlapig, Dr Luke Keeney, Professor Rick Valenta, Cong He, MLA staff and all their colleagues at the Sustainable Minerals Institute, The University of Queensland.

References

Albanese T and McGagh J (2011) Future trends in mining. In Darling P (ed) SME Mining Engineering Handbook, 3rd edn. Society for Mining, Metallurgy and Exploration, Inc., USA, pp. 21-36.

Alexander D, Bradshaw D, Manlapig E, Harbort G (2006) Froth Flotation. In Wills BA and Napier-Munn TJ (eds) Mineral processing technology: An introduction to the practical aspects of ore treatment and mineral, 7th edn. Butterworth-Heinemann, Oxford, pp. 267-352.

Barton P (1991) Ore textures: problems and opportunities. Mineralogical Magazine 55:303-315.

Carson DJ (1995) Geological-mineralogical controls on the metallurgical response of ores. Project Evaluation and Due Diligence short course, Prospectors and Developers Association of Canada, Ontario.

Darling P (2011) Mining: Ancient, modern and beyond. In Darling P (ed) SME Mining Engineering Handbook, 3rd edn. Society for Mining, Metallurgy and Exploration, Inc., USA, pp. 3-9.

Dusci M, Guibal D, Donaldson J, Voortman A (2007) Risk management through the use of 2D conditional Co-simulation at an underground gold Mine in Western Australia. In Dimitrakopoulos R (ed) Orebody modelling and strategic mine planning: Uncertainty and risk mangement models, 2nd edn. Spectrum Series, The Australasian Institute of Mining and Metallurgy, Victoria, pp. 103-110.

Evans C (2010) Development of a methodology to estimate flotation separability from ore microtexture. Dissertation, The University of Queensland.

Fandrich R, Gu Y, Burrows D, Moeller K (2007) Modern SEM-based mineral liberation analysis. Int J Miner Process 84:310-320.

Ferrara G, Preti U, Meloy TP (1989) Inclusion, shape, mineral texture and liberation. Int J Miner Process 27:295-308.

Gaudin AM (1939) Principles of mineral dressing. McGraw Hill, New York.

Jones MP (1987) Applied mineralogy - A quantitative approach. Graham and Trotman, London.

King RP (1994) Comminution and liberation of minerals. Miner Eng 7:12–140.

Lorenzen L and Barnard MJ (2011) Why is mineralogical data essential for designing a metallurgical test work program for process selection and design?. In Dominy DS (ed) The First AUSIMM International Geometallurgy Conference, The Australasian Institute of Mining and Metallurgy, Melbourne, pp. 163-172.

Petruk W (2000) Applied Mineralogy in the Mining Industry. Elsevier Science, The Netherlands.

Preti U, Ferrara G, Meloy T (1989) Influence of particle shape on liberation. Int J Miner Process 25:17-28.

Randolph M (2011) Current trends in mining. In Darling P (ed) SME Mining Engineering Handbook, 3rd edn. Society for Mining, Metallurgy and Exploration, Inc., USA, pp. 11-19.
Sutherland DN (2007) Estimation of mineral grain size using automated mineralogy. Miner Eng 20:452-460.
Sutherland DN, Gottlieb P (1991) Application of automated quantitative mineralogy in mineral processing. Miner Eng 4:753-762.
Tungpalan K, Wightman E, Manlapig E (2015) Relating mineralogical and textural characteristics to flotation behaviour. Miner Eng 82:136-140.
Tungpalan K, Wightman E, Manlapig E, Keeney L (2017) The influence of veins on miineral liberation as described by random masking simulation. Miner Eng 100:109-114.
Tungpalan K, Wightman E, Manlapig E (2018) The role of vein-type mineralization in mineral liberation. Miner Eng 116:209-212.
Williams SR and Richardson JM (2004) Geometallurgical mapping: A new approach that reduces technical risk. Proceedings of the 36th Annual Meeting of The Canadian Mineral Processors, Canadian Institute of Mining, Metallurgy and Petroleum, Ottawa, pp. 241-268.
Yingling JC (1990) Circuit analysis: Optimizing mineral processing flowsheet layouts and steady-state control specifications. Int J Miner Process 29:149-174.

A reliable method for the automated distinction of quartz gangue and epoxy resin with reflected light microscopy for geometallurgical characterisation

Ursula Grunwald-Romera, Juan Carlos Catalina, David Alarcón, Alfredo López-Benito, Ricardo Castroviejo
Universidad Politécnica de Madrid, Spain

Abstract. The reliable distinction of gangue (typically quartz or silicates) and epoxy resin (commonly used to embed the sample, before polishing) is a pending problem for the widespread automated mineralogical characterization of ores and its application to geometallurgy. Traditional methods based on specular reflectance (**R**) measures are not able to distinguish between gangue and resin because of their similar R values. Different additives (colorants and fluorescein) have been investigated to alter the spectral signature of the resin in polished thin sections. Automated segmentation can commonly be achieved with colour dyes, only if R ratios are used, instead of R values. However, the results are most reliable with the addition of fluorescein. The acquisition of fluorescence images with the 20x objective, shows a high contrast between bright and dark areas (belonging to resin and mineral particles, respectively). This opens the way to the generalized application of automated methods of optical microscopy, such as the AMCO system, for geometallurgical characterization, with a notable increase in efficiency over traditional methods (point counter) and a significant cost reduction compared to electron microscopy.

1 Introduction

The reliable distinction of gangue (typically quartz or silicates) and epoxy resin in reflected light microscopy (through the measurement of specular reflectance in the visible and near infrared ranges, between 400 and 1000 nm), is a common problem for the automated geometallurgical characterization of ores with digital image analysis software. This is not a difficult problem in polished whole rock samples, because resin is present at the border only and can be easily isolated.

In milled ore concentrates, however, each ore grain or particle is surrounded by resin. This resin must be discriminated from gangue in order to carry out automated quantitative analysis of ore and gangue, or when the contours of the grains have to be recognized to define morphological properties. This distinction is therefore a requirement for a widespread application of automated optical microscopy, which warrants a notable increase in efficiency over traditional methods (point counter) and a significant cost reduction compared to electron microscopy.

Neumann and Stanley (2008) studied the possibility of discriminating quartz from commercial epoxy resins. They concluded: "*The close coincidence of specular reflectance for quartz and epoxy resins ensures that there is not relevant reflectance contrast between them, even when spiked with dyes. This data set is final, and precludes the application of reflectance in light optical image analysis for assessment of liberation, phase quantification, or any other signal that requires separation of resin from transparent minerals*". Delbem et al. (2015) propose for iron ore characterisation a semi-automated quartz/resin classification, defining first the particle contours, and then applying the measured R values inside each particle to identify its components, but the contour definition is not always straightforward.

The approach of this work is the direct definition of the particles based on the measured R values.

2 Background

This research benefitted from previous experiences in the GeMMe Lab (University of Liège) and in the Laboratory of Applied Microscopy (**LMA**, Universidad Politécnica de Madrid), kindly contributed by Pirard E., and Pérez-Barnuevo L., resp., which even if unsuccessful were instrumental to avoid repetition of useless attempts, including use of organic solvents to etch the polished epoxy surface, laser ablation, use of different additives to modify the surficial appearance or the refractive index (and R) of the resin, use of different types of dyes (yellow, blue and red), graphite powder, etc.

A common feature of these attempts was the use of polished blocks (**PB**), in which results are usually unsatisfactory, even with coloured resins, because the epi-illumination penetrating the surface of the block is transmitted and diffused within the resin and the gangue, and can be finally conveyed back to the surface through the transparent gangue grains, apparently tinting them with the resin's colour.

In 2017, a Grade`s Thesis funded by a GIRMI-UPM grant (Grunwald-Romera 2017) brought forward Pérez-Barnuevo's work by studying the effect of different types of resin additives (the same yellow, red and blue dyes, plus fluorescein), in Polished Thin Sections (**PTS**). PTS have a typical thickness of 30 µm, thinner than the grain size of most samples, thus minimizing the presence of dyed resin under the grains. Should the grain size be smaller, thinner PTS might be prepared. This method proved to be quite effective, and therefore PTS were chosen as the standard sample preparation method for the tests that were performed later.

From 2016 to 2018, the LMA led the development of the AMCO System, an automated mineralogical characterisation system based on optical microscopy.

The work was carried out within a research project funded by EIT Raw Materials, with the participation of the University of Liège, the SME Thin Section Lab, and two mining companies (Cobre Las Cruces and KGHM). **AMCO** (which stands for Automated Microscopic Characterization of Ores), is the result of an upscaling of the CAMEVA system (Castroviejo et al. 2009, Catalina and Castroviejo 2017).

3 Materials and methods

A number of polished sections were prepared from two samples of quartz sand (IMOSAB and GUD), using two epoxy resins (Feroca and Struers EpoFix Kit), and four dyes from Struers: the three AcryDye pigment-based liquid colorants (yellow, red and blue), and EpoDye (fluorescein in powder). Undyed polished sections were also prepared, for comparison.

Nine PTS, two with each dye plus one without, and two PB, one with EpoDye and one undyed, were prepared from IMOSAB sand in the labs of Complutense University of Madrid (UCM) by the first author for her Grade's Thesis (2017). A set of polished sections used Feroca resin with 6 drops of AcryDye colorant for each one, while another set used EpoFix resin with 10 drops of AcryDye. For the sections with fluorescein, even if not exactly quantified, IMOSAB_F001 contained a larger amount of EpoDye than IMOSAB_F002.

Later on, five PTS and PB pairs from each sand sample (IMOSAB and GUD) were prepared at Thin Section Lab (Toul, France) using EpoFix resin and the same four dyes, plus one undyed.

Multispectral images of the polished sections were acquired at the LMA on a prototype of the AMCO system. The AMCO system prototype is based on a Leica DM6000 M reflected-light optical microscope integrating additional components, such as a fluorescence filter cube, a 12V/100W halogen light source with a custom hot mirror, a high-precision XY motorized stage, a filter wheel containing a large number of hard coated bandpass filters in the VNIR range, and a high-resolution monochrome video camera. The multispectral images are typically composed of 21 bands: 13 reflectance bands in the visible range from 400 to 700 nm with 25 nm bandpass (**BP**), 6 reflectance bands in the NIR from 750 to 1000 nm with 50 nm BP, a reflectance band in the NUV range centred at 370 nm with 36 nm BP, and an optional fluorescence band obtained through the L5 cube (excitation filter: BP 480/40 nm, dichromatic mirror: 505 nm, suppression filter: BP 527/30 nm), which is especially suited for fluorescein.

4 Multispectral measurements

Multispectral images of each of the polished sections were acquired with 5x, 10x and 20x objectives. For the images of the coloured resin sections, just the 20 reflectance bands were captured, as these resins do not exhibit significant fluorescence. However, for the images of the fluorescent resin sections, all the 21 bands (20 reflectance bands plus the fluorescence band) were captured. The fluorescence band does not measure reflectance, but the intensity of the fluorescence of the sample. Because of this, it was necessary to adjust the integration time of the camera for the fluorescence band before the acquisition, to adapt it to the brightness level of the fluorescent resin, which depended on the amount of EpoDye added (higher amounts of fluorescein made the resin shine brighter, so it needed a shorter exposure time to prevent the image from becoming saturated).

Several images of each PB and each PTS were acquired with each objective, in order to determine the effect of the different dyes on the resin. These images were examined one by one with the AMCO image analysis software (Fig. 1). In each image, a number of rectangular boxes were manually drawn with the mouse on sufficiently uniform regions of the sand grains and the resin matrix, in order to select the gangue and resin regions used to conduct the study.

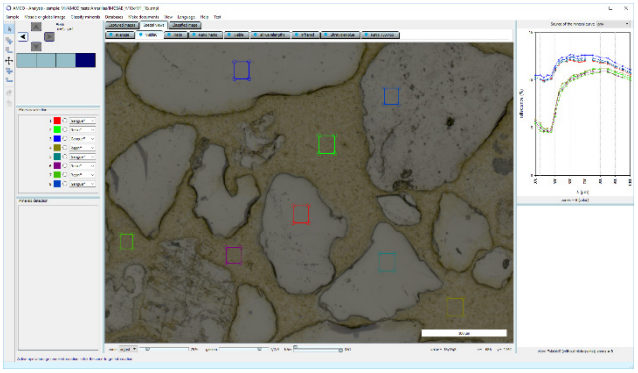

Figure 1. Window capture of AMCO image analysis software while examining an image of a polished thin section (IMOSAB-Y001)

The top-right graph of Figure 1 shows spectral curves measured on an image of a PTS prepared with yellow dye. Each curve is computed as the average (or the mode, at user's choice) of the multispectral R values of all the pixels contained within a region. The measured R values correspond in fact to apparent reflectance, which is higher than the nominal specular reflectance due to the well-known contribution of light diffused within the polished section (Criddle 1990). This effect is produced in transparent minerals by internal reflections, which are seen through the surface.

Measurements on PB show that the R values are very similar for gangue and resin, making automated distinction unreliable, while for PTS there are noteworthy differences. Therefore, for the rest of the discussion we will focus on PTS only.

5 Results and discussion

Figure 2 shows average spectral curves for gangue and resin from PTS prepared with resin dyed with the three colorants. Studying the curves, it can be realised that the R values of dyed resin regions are somewhat lower than the R values of gangue regions at some bands. These bands are typically the bands near the complementary colour of the dominant hue of the dye. For instance, with the yellow dye, resin appears significantly darker than

gangue in the bands closer to the blue range (between 400 and 500 nm).

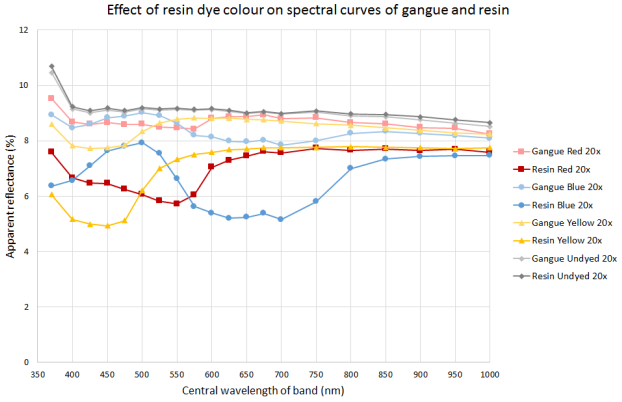

Figure 2. Effect of resin dye colour on measured spectral curves of gangue and resin

This spectrally uneven darkening of the resin can be exploited by computing ratio images of selected bands. Figure 3 shows a ratio image, in which each pixel is the quotient of the R value of the 425 nm band divided by the R value of the 700 nm band, for a PTS made with yellow-dyed resin. The difference in grey level between the gangue and the resin in this image is remarkable, as the bimodal histogram in Figure 4 clearly shows.

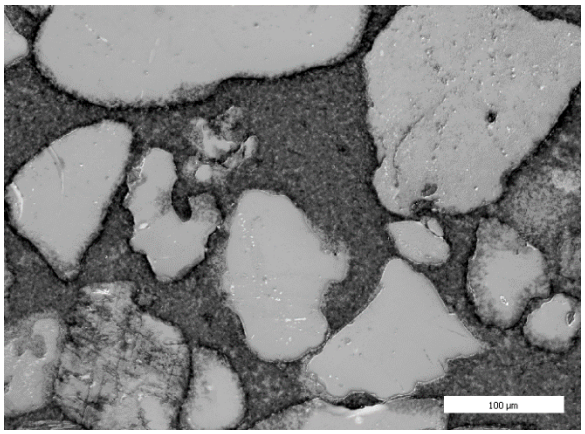

Figure 3. Ratio of 425 / 700 nm bands (yellow-dyed resin, 10x)

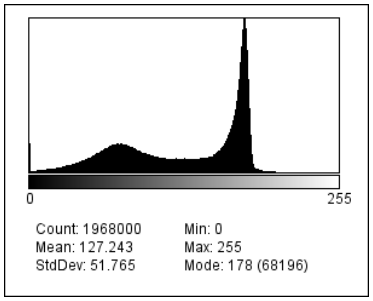

Figure 4. Histogram of the 425 / 700 nm ratio image of Figure 3

The behaviour of the three AcryDye colorants is similar, although the effect is less intense for the red and blue dyes than for the yellow. Depending on the amount of colorant added, the aspect of the resin can change considerably. If the amount of dye is small, its pigments absorb part of the light that impinges on the resin, decreasing its apparent reflectance. As the amount of pigment increases, its particles make the resin behave like a higher-reflectance surface.

The magnification of the objective also has a clear effect in the separation between the spectral curves of gangue and resin: it is wider for the 5x and 10x objectives than for the 20x objective (Fig. 5). Nevertheless, 20x is the preferred magnification for ore characterisation, so the selected solution should be the one working best with 20x objectives.

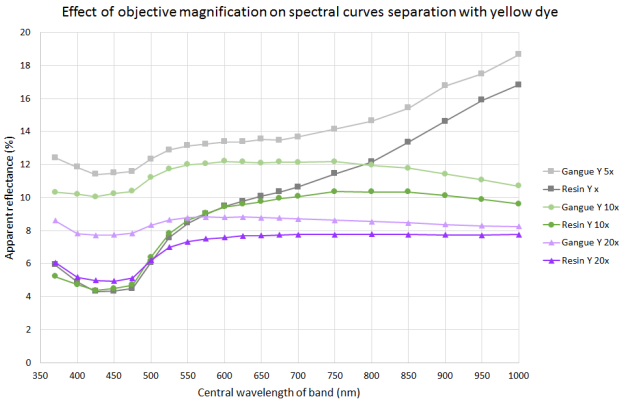

Figure 5. Effect of objective magnification on spectral curves separation

EpoDye behaves as a colorant very similarly to the yellow dye, and produces very good ratio images as well. However, its effect is even more outstanding when the image is acquired in fluorescence mode, as the resin appears bright while the gangue looks almost black, as Figure 6 shows. The histogram of fluorescence images is clearly bimodal (Fig. 7), implying a straightforward segmentation.

Therefore, the best solution is to use fluorescein as dye (EpoDye), and acquire a band in fluorescence mode, because of its higher effectivity with the 20x objective. While in bright-field mode differences between gangue and resin are small, in fluorescence mode resin becomes very bright and is clearly distinguished from mineral grains. Fluorescent minerals that might exist in the sample could be the only disadvantage of this method, but they are not common components of milled ore concentrates, and their fluorescence would also help to detect them.

6 Conclusion and applications

The results of this work for Polished Blocks (PB) agree with the conclusions reported by Neumann and Stanley (2008).

However, our work has shown that an effective method to distinguish between resin and gangue minerals is possible for Polished Thin Sections (PTS), without altering the properties of the ores or the gangue present in the sample.

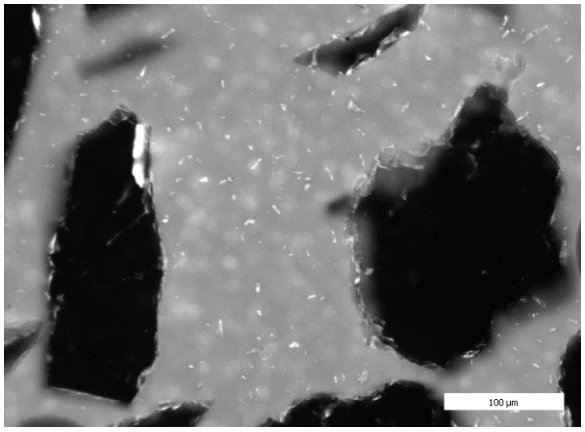

Figure 6. Image of fluorescence (fluorescein-dyed resin, 20x)

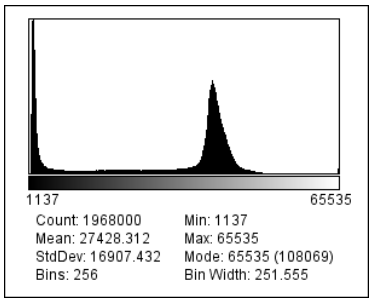

Figure 7. Histogram of the fluorescence image of Figure 6

Although all the studied colorant dyes can provide ratio images presenting a good discrimination between resin and gangue with 5x or 10x objectives, the best solution appears to be the use of the fluorescent dye, because of its high effectivity with the 20x objective, both for ratio and fluorescence images. This enables the application of Digital Image Analysis based on Reflected Light Microscopy to milled ore samples or concentrates.

With this solution, using PTS, the way to the generalized application of automated methods of optical microscopy for geometallurgical characterization is wide open. Nevertheless, for whole-rock studies automated identification of gangue minerals is possible even in PB, except for porosity measurement or for very porous samples, because the presence of resin is limited to the borders and can be easily isolated.

Figure 8. Mask for resin computed from image of Figure 6

The AMCO image analysis software incorporates a routine to implement the automated distinction between gangue and resin that creates a mask for the resin area, isolating the particles present in the microscopic field (Fig. 8). AMCO is thus able to offer an accurate modal analysis of milled ore concentrates, as well as whole-rock samples, automatically discounting the regions of resin from the sample.

Acknowledgements

This study has been undertaken as a UPM Grade Thesis and as a contribution to one of the scheduled tasks of AMCO (EIT Project no. 15039. 2016-2018), R+D+i Project funded by EIT Raw Materials, EU- H2020 Program. The colleagues of the AMCO Consortium (particularly TSL and E. Pirard and his ULiège team) and of the Sample Preparation Lab of the Department of Geochemistry and Petrology (Faculty of Geological Sciences, Madrid Complutense University) are thankfully acknowledged.

EIT RawMaterials is supported by the EIT, a body of the European Union

References

Castroviejo R, Brea C, Pérez-Barnuevo L, Catalina JC, Segundo F, Bernhardt HJ, Pirard E (2009) Using computer vision for microscopic identification of ores with reflected light: preliminary results. Pp. 682-684, in: Williams et al., eds. Smart Science for exploration and Mining (Proc.10th biennial SGA Meet. Vol. 2. Townsville, Australia), ISSN: 9780980558685.

Catalina JC and Castroviejo R (2017) Microscopía de Reflectancia Multiespectral: Aplicación al Reconocimiento Automatizado de Menas Metálicas. Rev. Metal. 53 (4):1-20. ISSN 0034-8570. doi: http://dx.doi.org/10.3989/revmetalm.107.

Criddle A (1990) Microscope photometry, reflectance measurement, and quantitative colour. Chapter 6, pp. 135-169, in Jambor JL and Vaughan DJ, editors: Advanced Microscopic Studies of Ore Minerals. MAC Short Course 17, Ottawa.

Delbem ID, Galéry R, Brandao PRG, Peres AED (2015) Semi-automated iron ore characterisation based on optical microscope analysis: quartz/resin classification. Miner. Eng. 82:2-13.

Grunwald-Romera, U (2017) Detección de ganga en concentrados de planta por microscopia óptica de reflexión mediante métodos automatizados. Proyecto Fin de Carrera / Trabajo Fin de Grado, E.T.S.I. de Minas y Energía (UPM). http://oa.upm.es/48414/

Neuman, R and Stanley, C J (2008) Specular reflectance data for quartz and some epoxy resins - Implications for digital analysis based on reflected light optical microscopy. Ninth International Congress for Applied Mineralogy, Brisbane 703-705.

Gold and silver mineralogy of the Liikavaara Cu-(W-Au) deposit, northern Sweden

Mathis Warlo, Christina Wanhainen, Glenn Bark
Division of Geosciences and Environmental Engineering, Luleå University of Technology, Sweden

Peter Karlsson
Exploration Department, Boliden AB,

Abstract. The Liikavaara Cu-(W-Au) deposit in northern Sweden is scheduled for production by the mining company Boliden AB in 2023. The ore will be processed in the plant of the nearby Aitik Cu-Au deposit. Copper will be the primary product and the trace metals Au and Ag will be byproducts. The trace mineralogy of Liikavaara, however, differs from that of Aitik and this might have implications on the mineral processing and recovery efficiency. Gold occurs mostly as free <10 µm-sized grains of native Au and electrum. Some Au is associated with native Bi, typically in <5 µm Bi-melt drops. Gold grains commonly form inclusions in quartz and sulfide minerals. Silver is found in electrum, hessite and acanthite. Hessite is the most abundant Ag mineral and it is commonly intergrown with pilsenite. Similar to Au, inclusions and crack-fillings of Ag in sulfides and quartz are most prominent. The small grain size, the diverse mineralogy, the association with Bi-phases, and the occurrence as inclusions in quartz may lower the recovery of Au and Ag in Liikavaara compared to Aitik, where Au and Ag phases are mostly bound in sulfides. Hence, adaptation of the processing parameters may be necessary in order to increase recovery of Au and Ag from the Liikavaara ore.

1 Introduction

The mineralogy, occurrence and distribution of trace metals in ore deposits often hold valuable information on ore genesis, but also their study is of interest from an economic perspective. Despite their low abundance, they can have a strong impact on the profitability of a mining venture. Trace metals like Au and Ag commonly add value as byproducts in mining operations. Other metals like Sb, As and U are deleterious. They either lower the quality of a primary commodity or require costly remediation to comply with environmental regulations. A good understanding of the trace metal mineralogy and its distribution in an ore deposit is therefore crucial to optimize profit and increase sustainability of a mining operation.

The Liikavaara Cu-(W-Au) deposit is an intrusion-related vein-style ore deposit in northern Norrbotten, Sweden (Fig. 1). It has a total resource estimate of 57.5 kton at 0.26% Cu, 0.06 g/t Au, and 2.2 g/t Ag (Boliden AB summary report 2018). Boliden AB holds the mining concession for the deposit and is currently in the mine development stage with estimated production to start in 2023. The deposit is enriched in a number of trace metals including Bi, Au, Ag, Sn, Te, and W. Gold and Ag are to be produced as byproducts next to the primary production of Cu. Tungsten and other trace metals are currently not deemed profitable to extract. The Liikavaara ore will be processed in the plant of the nearby Aitik Cu-Au deposit. Despite their proximity, the two deposits show some differences in their mineralization (Warlo et al. submitted). This might affect the behavior of the ore during processing and ultimately the recovery efficiency. While the Aitik deposit has been described geologically in several studies (Monro 1988, Wanhainen 2005, Sammelin-Kontturi et al. 2011, Wanhainen et al. 2014), literature on the Liikavaara deposit are limited (e.g. Zweifel 1976, Warlo et al. submitted). Here, we present a detailed characterization of Au and Ag mineralogy in the Liikavaara deposit. The results should aid to optimize recovery efficiency of Au and Ag from the Liikavaara ore.

2 Geological background

The Liikavaara Cu-(W-Au) deposit is situated in the Gällivare area of the ore district of Northern Norrbotten, close to the world-class Aitik Cu-Au deposit (Fig. 1A). The deposit is situated in the eastern limb of a south-southeast dipping syncline and extends for about 1 km along strike, at a width of 100 m (Zweifel 1976). The ore body dips 80°W and is known to at least 400 meters depth (Zweifel 1976) (Fig. 1C, D). The ore is hosted by a metadiabase, which is partly altered and metamorphosed to biotite schist. The metadiabase intruded between metavolcaniclastic wall rocks ranging in composition from andesitic to basaltic (Estholm 2014, Warlo et al. submitted) (Fig. 1B–D). The rocks belong to the Muorjevaara Group and are of Svecofennian age (Zweifel 1976; Martinsson & Wanhainen 2004). A 1.87 Ga granodiorite intrusion in the footwall is suggested to be responsible for ore genesis and aplite dikes cutting the host rocks acted as pathways for the ore fluids (Fig. 1B–D) (Warlo et al. 2017, Warlo et al. submitted). Mineralization occurs predominantly in veins of quartz-tourmaline and calcite (Warlo et al. 2017, Warlo et al. submitted). Major ore minerals are chalcopyrite, pyrite, and pyrrhotite. Sphalerite, galena, scheelite, molybdenite, marcasite and magnetite are minor ore minerals. Whole-rock analyses show Bi, Au, Ag, Sn, and W to be prominent trace metals. Bismuth mineralogy is diverse and includes native Bi, Bi-tellurides and Bi-sulfides. Gold occurs as native Au and as grains of electrum. Silver is besides in electrum also found in hessite and acanthite. Tin occurs only in cassiterite and W in scheelite (Warlo et al. submitted). Warlo et al.

(submitted) present a paragenetic sequence where magnetite was formed first, followed by chalcopyrite, pyrite, and pyrrhotite. The minor sulfides formed later and the trace metal phases formed in an even later stage. Remobilization of the primary mineralization by hydrothermal fluids similar to the conditions in the Aitik deposit (Wanhainen & Martinsson 2003) is likely.

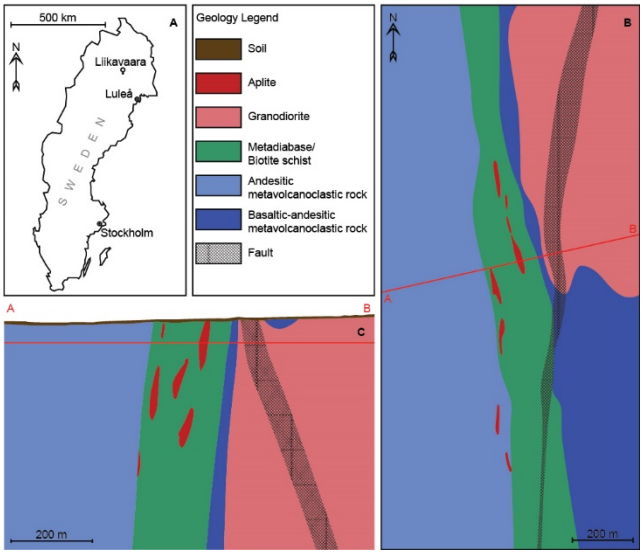

Figure 1. Geological map and profile of the Liikavaara Cu-(W-Au) deposit. **A**. Location of the deposit in northern Norrbotten, Sweden. **B**. Plan view of the Liikavaara Cu-(W-Au) deposit, at 100 m below surface. **C**. Cross section through the deposit (modified from Warlo et al. submitted).

3 Methods

In this study, sixteen thin section samples from the Liikavaara Cu-(W-Au) ore deposit were studied by light optical microscopy (LOM) and scanning electron microscopy (SEM).

Geochemical assays were used to select suitable drill core samples enriched in the targeted trace metals. Polished thin sections were prepared by Vancouver Petrographics LTD. The thin sections were studied with a Nikon ECLIPSE E600 POL optical microscope, in both transmitted and reflected light. Regions of interest were subsequently analyzed with a Zeiss Merlin FEG-SEM-EDS/WDS. Imaging was done in both secondary and backscattered electron mode.

4 Results

4.1 Gold

Gold in Liikavaara occurs in quartz-sulfide-tourmaline veins as native Au and electrum (Fig. 2A–D). Differentiation between the two phases is solely based on the Au/Ag ratio (anything >20% Ag is classified as electrum). Gold grains are typically <10 µm in size. They form rounded to angular grains and are partly elongated. The Au grains occur as inclusions and crack-fillings in especially quartz but also in the sulfides sphalerite, pyrite, and molybdenite (Fig. 2A–C). In places, they can also be found spatially close to scheelite and tourmaline. Some of the Au grains are associated with Bi-minerals, especially native Bi and pilsenite (Bi_4Te_3) (Fig. 2A). For some Au grains, native Bi occurs in the form of melt-droplets with Au partitioning at the rim (Fig. 2D). These Bi-droplets are generally <5 µm and only observed in quartz.

4.2 Silver

The dominant Ag minerals in Liikavaara are hessite (Ag_2Te), electrum and acanthite (Ag_2S) (Fig. 2E, F). Similar to Au, the occurrence of Ag minerals is limited to veins of predominantly quartz and sulfides. Hessite occurs mainly tightly intergrown with pilsenite and occasionally with volynskite ($AgBiTe_2$). Hessite also forms inclusions at the rim of especially chalcopyrite but also other sulfides (Fig. 2E). At these sulfide rims hessite is commonly also in contact with calcite and tourmaline. Hessite grains vary in size from a few microns up to 100 µm. Acanthite is less common compared to hessite and the maximum observed grain size is ~30 µm. It occurs anhedral at the border of sulfide grains like pyrite and chalcopyrite and in contact with silicates (e.g. chlorite, tourmaline, quartz) and carbonates (e.g. calcite, ankerite) (Fig. 2F). The character and occurrence of electrum is described in 4.1.

5 Discussion

Introduction of Au- and Ag-minerals to the Liikavaara ore zone have previously been discussed to be the result of Bi-melt scavenging of Au and Ag from the footwall intrusion and subsequent deposition in veins in the ore zone (Warlo et al. submitted).

In the nearby Aitik deposit, Au occurs as native Au, electrum and amalgam, where electrum and amalgam are mostly found with sulfides, and native Au is typically associated with silicates. Gold grains are commonly <10 µm, but grains up to 35 µm have been observed (Wanhainen et al. 2003, Sammelin-Kontturi et al. 2011). Spatial variations in Au composition have been described, such as Ag-rich electrum and native Au common at depth and Au-rich electrum more distal to the core of the deposit (Sammelin-Kontturi et al. 2011). Sammelin-Kontturi et al. (2011) suggest this to possibly reflect differing conditions of Au/Ag deposition within the post-ore hydrothermal system but also highlight the possibility of multistage Au mineralization due to an IOCG (Iron Oxide Copper Gold) overprint at Aitik.

In Liikavaara no relationship between compositional and spatial variation of Au and Ag has been observed on deposit-scale. However, a contrast exists between round grains of native Bi with partitions of Au in quartz and partly elongated crack-infillings of electrum in sulfides. Furthermore, hessite and acanthite are mostly observed at the border of sulfides. This difference in character and occurrence of Au and Ag, in silicate and sulfide minerals in Liikavaara could indicate a multistage mineralization of Au and Ag similar to Aitik. Aside from Bi-melt scavenging, remobilization of Au and Ag from primary sulfides could

also have been a process involved in Au and Ag mineralization in Liikavaara.

Regarding mineral processing at the Aitik mine, the present method for Au and Ag recovery is Cu-flotation. This means the Au and Ag are floated with the copper minerals and later separated from the concentrate. Since the ore from Liikavaara will be processed in the Aitik plant, a portion of Au from the Liikavaara ore will likely be lost to the tailings. This is due to the small Au grain size that limits floatability and the association with silicates that causes Au to go with the gangue.

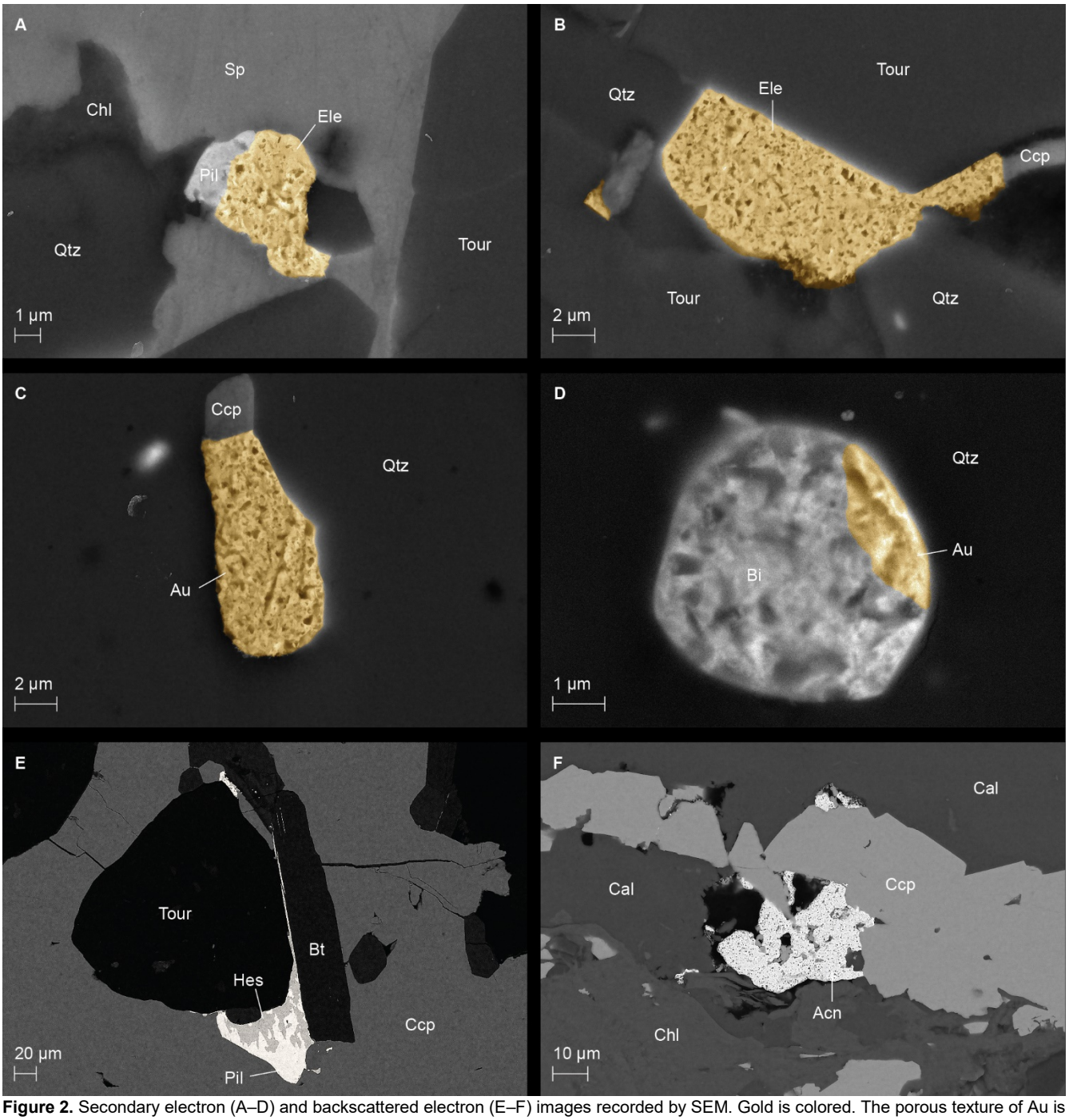

Figure 2. Secondary electron (A–D) and backscattered electron (E–F) images recorded by SEM. Gold is colored. The porous texture of Au is partly natural and partly an artefact of polishing. **A**. Electrum associated with sphalerite and pilsenite. **B**. Electrum and chalcopyrite associated with tourmaline and quartz. **C**. Native Au associated with chalcopyrite in quartz. **D**. Bismuth melt drop with Au, in a quartz matrix. **E**. Hessite intergrown with pilsenite at the boundary to chalcopyrite. **F**. Acanthite associated with chalcopyrite, calcite and chlorite. Abbreviations: Acn – acanthite, Au – gold, Bi – bismuth, Bt – biotite, Cal – calcite, Ccp – chalcopyrite, Chl – chlorite, Ele – electrum, Hes – hessite, Pil – pilsenite, Sp – sphalerite, Tour – tourmaline, Qtz – quartz

At present, it is likely that only the Au bound in sulfides will be recovered. Silver may have a higher chance for recovery. Acanthite and hessite are commonly associated with sulfides and grains are often >10 µm. However, hessite is mostly complexly intergrown with pilsenite, which may limit liberation and introduce unwanted Bi to the concentrate.

For a proper prediction of trace metal deportment during processing and a potential environmental impact more work is necessary. While samples were collected across the deposit, total sample volume was low and not all samples contained grains of Au and Ag. Therefore, to support representativeness of the findings of this study statistical analysis is required. For this, future work with automated quantitative mineralogy is planned. The characterization of Au and Ag mineralogy presented here provides an important basis to successfully plan and carry out quantitative analysis of the various minerals and textures.

Acknowledgements

Boliden AB is acknowledged for financing the analytical work in this study, which is part of a PhD project financed by CAMM^2 (Centre of Advanced Mining and Metallurgy), Luleå University of Technology. We gratefully thank Boliden AB for their continuous support and involvement in the project and for the permission to publish this abstract.

References

Estholm M (2014) Identification of the host rocks and the environment of formation of the Liikavaara Cu-Au deposit, Norrbotten, Sweden. Bachelor thesis, Stockholm University

Martinsson O, Wanhainen C (2004) Character of Cu-Au mineralizations and related hydrothermal alterations along the Nautanen deformation zone, Gällivare area, northern Sweden. Econ Geol 33:149-160

Monro D (1988) The geology and genesis of the Aitik copper–gold deposit, Arctic Sweden. Dissertation, University of Wales, College of Cardiff

Sammelin-Kontturi M, Wanhainen C, Martinsson O (2011) Gold mineralogy at the Aitik Cu-Au-Ag deposit, Gällivare area, northern Sweden. GFF 133:1-12

Wanhainen C, Kontturi M, Martinsson O (2003) Copper and gold distribution at the Aitik deposit, Gällivare area, northern Sweden. Appl Earth Sci, 112(3):260-267

Wanhainen C, Martinsson O (2003) Evidence of remobilisation within the Palaeoproterozoic Aitik Cu-Au-Ag deposit, northern Sweden: A sulphur isotope study. In: Proceedings of the 7th biennal SGA meeting, Athens, pp 1119-1122

Wanhainen C (2005) On the origin and evolution of the Palaeoproterozoic Aitik Cu-Au-Ag deposit, northern Sweden: a porphyry copper-gold ore, modified by multistage metamorphic-deformational, magmatic-hydrothermal, and IOCG-mineralizing events. Dissertation, Luleå University of Technology

Wanhainen C, Nigatu W, Selby D, McLeod C, Nordin R, Bolin N-J (2014) The distribution, character, and rhenium content of molybdenite in the Aitik Cu-Au-Ag-(Mo) deposit and its southern extension in the northern Norrbotten ore district, northern Sweden. Minerals 4:788-814

Warlo M, Martinsson O, Wanhainen C, Karlsson P, Höglund S (2017) Mineralisation paragenesis of the Liikavaara Cu-(W-Au) deposit, northern Sweden. In: 14th SGA Biennial Meeting on Mineral Resources to Discover, Quebec City, pp 971-974

Warlo M, Wanhainen C, Martinsson O, Karlsson P (2019) Mineralogy and origin of the intrusion-related Liikavaara Cu-(W-Au) deposit, northern Sweden. Submitted to GFF

Zweifel H (1976) Aitik - geological documentation of a disseminated copper deposit: a preliminary investigation. SGU C720, 80 pp

Geochemistry and quantitative mineralogy of REE-bearing phosphate stockpile ore from the Catalão Region, Brazil

Tim Rödel, Gregor Borg
Institute of Geosciences and Geography, Martin Luther University Halle-Wittenberg, Germany

Abstract. In this ongoing study, raw materials are being investigated for their potential as rare earth element (REE) sources. Amongst other sample groups, REE-mineral-bearing phosphate stockpile ore is analysed with respect to its quantitative mineralogical distribution and geochemical composition. Laser granulometry, ICP-MS geochemistry, SEM-EDX, and automated mineralogy tools are currently used. Total rare earth oxide (TREO) concentrations are as high as 0.7% to 0.9% but may reach up to 1.8%. Determining the fraction of extractable element content from a geometallurgical point of view is one major goal of the study. The phosphate ore consists predominantly of apatite, Fe-oxide minerals (hematite, magnetite, minor goethite) intergrown with ilmenite, quartz, and phyllosilicates like phlogopite or vermiculite. Minor, variable amounts of gorceixite, carbonates, rutile, and barite occur locally. Accessory heavy minerals are pyrochlore, Ba-pyrochlore, zirconolite, and baddeleyite. The main REE ore mineral is the REE-phosphate monazite with varying Ce-La-Nd proportions. Minor amounts of REE are also bound to pyrochlore, apatite, and zirconolite.

1 Preface

The REE have been classified as critical raw materials in 2014 due to supply risk, low end of life recycling rate and economic value (European Commission 2014). Important applications are diverse and uses in metallurgy as alloys, strong magnets (especially Nd-F-B magnets), ceramics or electronics (resistor materials) are common (Krishnamuthy and Gupta 2016). Diversifying the supply of critical elements for the European market is crucial in securing the future development of high-tech industries and limiting supply risks. The beneficiation of by-products from raw material production, tailings, and industrial residues (Binnemans 2015) enables society to pursue sustainable development by feeding previously unused resource potential into the economic value chain. Employing environmentally friendly processes without additional mining, reduces the ecological footprint, whilst improving economic profitability. As demonstrated by Pereira et al. (2019) assessing the geometallurgical properties of REE-bearing material might be useful in determining its economic potential as a by-product.

The recovery of REE as a by-product from phosphoric acid production for the fertilizer industry from the Catalão Region is the overall goal of the current study. Habashi (1984) estimated a possible global supply of 500,000 t of REE from 130 million t of annually treated phosphate rock based on a TREO content of up to 1%. Brazil hosts an estimated phosphate reserve of 170 million t with an annual production of 5.4 million t (U.S. Geological Survey 2019). Consequently, a potential of an annual production of up to 25,000 t REE was estimated by Bardano and Gomes (2015) for sources from the Brazilian phosphate industry.

The run-of-mine stockpile phosphate ore from the Catalão Region presented here hosts the base inventory of available REE-mineral phases at the beginning of the process from ore to waste. Material streams during phosphate beneficiation including tailings are currently also investigated. Evaluating the source material's mineralogical composition is critical for selecting and optimizing further mineral beneficiation processes. One key objective of the current study is a comprehensive mineralogical description and assessment of the quantitative distribution of available mineral phases with regard to element recoverability and possible unwanted gangue. This includes particle size distribution, element composition of identified phases, and mineral intergrowth ("liberation").

2 Samples and methods

The analysed phosphate ore represents weathering products of alkaline igneous rocks from the Catalão Region, Brazil. Samples have been taken from pre-crushed blended stockpile material before phosphate beneficiation. Because of the unrefined nature, 60 % of the material is generally larger than 250 µm. Due to limited sample material available, no full sieving analysis was performed. Only the sample fraction passing 250 µm mesh was analysed using granulometry (Fig. 1).

The particle size distribution analyses were performed using a Cilas 920 laser diffraction granulometer with sample material in isopropanol suspension to prevent agglomeration of fine particles. Sieving lines of the analysed samples exhibit a similar shape and therefore similar characteristics. The grain size distribution is broad and 25 to 35 % of the analysed material is smaller than 25 µm. It was suspected that accessory heavy minerals are accumulated in the fine fraction below 80 µm. The particle size distribution analyses were performed using a Cilas 920 laser diffraction granulometer with sample material in isopropanol suspension to prevent agglomeration of fine particles.

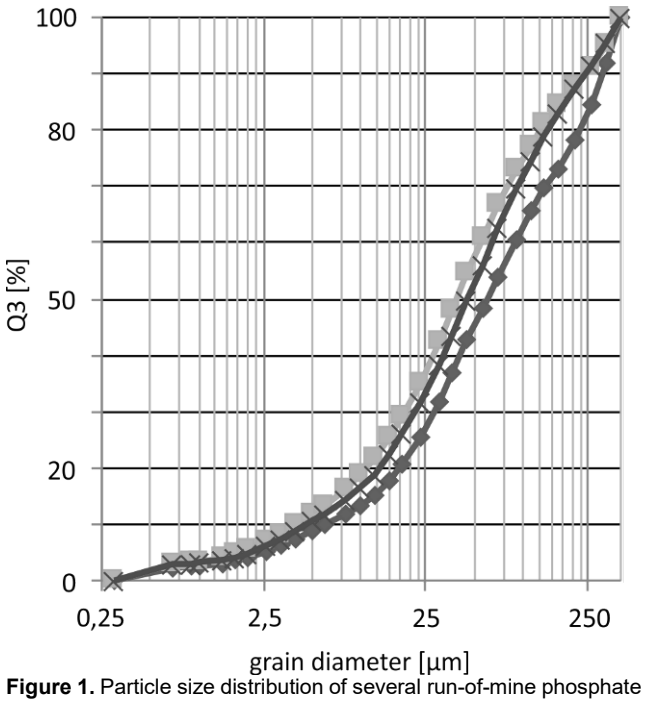

Figure 1. Particle size distribution of several run-of-mine phosphate ore samples passing 250 µm mesh. The cumulative sieving curve was created based on laser granulometry.

Sieving lines of the analysed samples exhibit a similar shape and therefore similar characteristics. The grain size distribution is broad and 25 to 35 % of the analysed material is smaller than 25 µm. It was suspected that accessory heavy minerals are accumulated in the fine fraction below 80 µm. For this reason, special emphasis was put on fine particle analysis. Grain mounts of representative sample splits from untreated samples, as well as milled and sieved (<125 µm mesh) material were prepared. Due to the heterogeneous particle size distribution, the subsequent additional sample preparation step proved necessary to achieve a homogeneous particle distribution in the granular polished sections. These will in turn improve the representability of the analysis using SEM-based automated mineralogy. Tests show that the results of the mineral distribution analysis for minerals occurring as large particles like Fe-oxides, quartz, or apatite have a much higher coefficient of variation (2- to 4-fold) in the untreated raw samples compared to milled and sieved material. Thus the absolute variations between individual measurements could be dramatically reduced by further crushing and sieving. For evaluating mineral and particle associations, the polished sections of raw untreated sample material remain of high importance nonetheless. Special precautions for avoiding nugget effects have to be taken, when working with this kind of heavy mineral target fraction.

Mineral distribution analyses were performed using the SEM coupled Bruker Quantax “feature analysis” tool and the “Advanced Mineral Identification and Characterization System” (AMICS). Both automated software tools are based on the collection of EDX spectra from segmented BSE greyscale images. Whereas the Bruker “feature analysis” tool is based on spectra quantification, the AMICS system uses spectra shapes to match measured references. To this end a new database with relevant mineral phases was created for both systems to allow successful classification of detected spectra. Whereas Bruker “feature analysis” represents a more conservative particle counting approach, AMICS is a sophisticated software package based on MLA code. Compared to quantitative XRD with Rietveld method the techniques mentioned above allow a quantification of multiphase mineral systems (>10 phases), accessory minerals (content below 1 %), or poorly crystalline phases. Additionally, information regarding mineral particle properties like size and liberation is generated. The mineral content can be expressed as area-, volume-, or weight-percent. Area percent is the actual measured particle property, based on segmented pixels, whereas volume is derived from a spherical model of the measured 2 D mineral area. Weight percent (wt %) is calculated from volume and mineral density. In this text mineral fractions are expressed as area %.

The geochemical analyses for major and trace elements were performed at the commercial laboratory “ALS Minerals”, Ireland using ICP-OES and ICP-MS. Digestion was achieved following lithium borate fusion. Non-destructive geochemical screening of sample material was achieved by portable XRF analysis with a ThermoScientific Niton Xl3t.

3 Geochemical and mineralogical properties of stockpile phosphate ore

The investigated stockpile phosphate ore samples have a complex mineralogical composition and broad particle size distribution. Although homogenised after the mining operation, blending of the primary phosphate ore from different mining levels may result in variable geochemistry and mineralogy. Preliminary results of drill core material from different ore zones show a high variability in element composition and mineral inventory (Maak et al. 2019).

Major element concentrations of the selected and examined samples up to date are characterised by high Fe_2O_3 with 37 to 44% followed by CaO with 16 to 21%, SiO_2 with 15 to 18% and P_2O_5 with 12 to 16% (Fig. 2). Ba contents are generally elevated between 6000 to 9000 ppm, whereas Sr concentrations reach 3000 to 5,000 ppm. Nb contents of the analysed samples are as high as 2000 to 2,500 ppm but commonly above the detection limit (>2,500 ppm). TREO concentrations range between 0.7% to 0.9% but may reach up to 1.8%. These variations have to be considered when estimating the total rare earth element content available for further beneficiation. Generally, LREE exhibit a distinct enrichment compared to HREE. Ce, La, Nd and Pr are quantitatively the dominant REE.

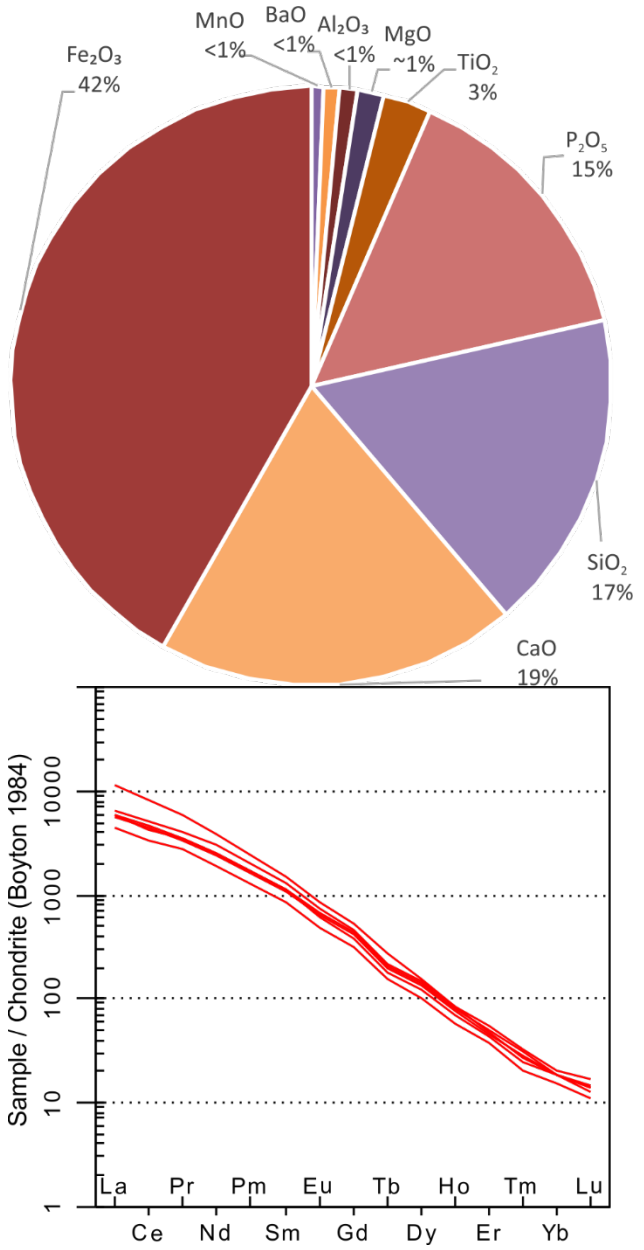

Figure 2. Mean concentration of major elements (see text for further explanation) and chondrite-normalized REE-patterns (Boyton 1984) for analysed stockpile ore samples.

Fe-oxide minerals (29-38% total area), apatite (32-39% total area), and quartz (19-23% total area) constitute the predominant rock forming mineral groups of the examined samples, which is in good accordance with the major element composition. Fe-oxides consist of varying amounts of martitised magnetite, hematite, goethite, and limonitic mixtures of goethite and clay minerals. Based on SEM-EDX analyses, Fe-carbonates like siderite are difficult to differentiate from Fe-oxide minerals but minor amounts of ankerite are easily distinguished by the presence of Ca in the spectra. Locally, Fe oxide minerals occur as large particles, intergrown with all occurring mineral phases, especially with quartz and apatite (Fig. 3). Ilmenite commonly occurs intergrown and overgrown by Fe-oxide minerals (most likely hematite) as fine exsolution lamellae. Species of Mg-bearing ilmenite have also been detected. Total ilmenite content is relatively low between 1.5% to 3%. Other Ti-bearing minerals like titanite or rutile rarely make up more than 0.1% of the total mineral portion. Rutile primarily occurs as a Nb-bearing variety.

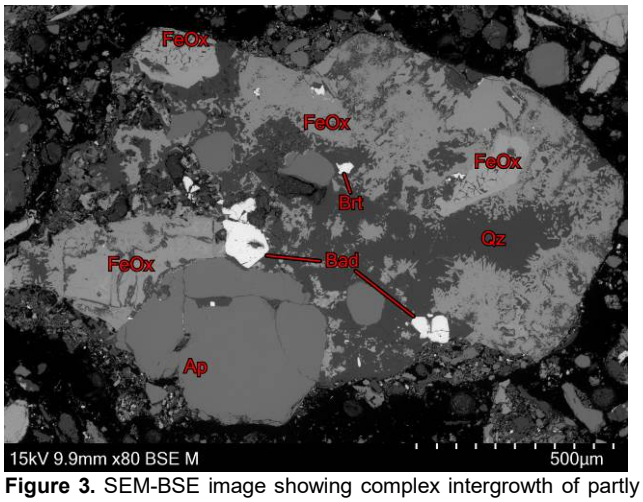

Figure 3. SEM-BSE image showing complex intergrowth of partly euhedral specular Fe-oxide minerals (FeOx) with quartz (Qz), subhedral apatite (Ap) and heavy minerals like baddeleyite (Bad) and barite (Brt).

The main phosphate carrier of the investigated samples is apatite with a P-80 between 205 and 950 µm. In the raw stockpile run-of-mine ore 55 to 70% of the total area of apatite particles are already liberated. Peculiar is its intergrowth and overgrowth of smaller Ba-alumophosphates (gorceixite). This mineral is occurring in low concentrations between 1 and 1.5% of the observed mineral particles. The presence of REE in apatite was detected but low concentrations prevent a semi-quantitative analysis using EDX.

Quartz occurs as particles with a P-80 between 325 and 770 µm. It appears as single particles but more commonly is intergrown with Fe-oxides or apatite. Quartz typically forms massive particles encapsulating euhedral apatite or specular hematite or as cementitious texture filling of fractures between larger apatite particles or Fe-oxides. Other silicates occur with varying combined quantities between 1.5 and 3%. Most common are Mg-bearing phyllosilicates like phlogopite, vermiculite, or chlorite. Carbonates are mainly represented by dolomite and only minor calcite.

Interesting from a raw material point of view are accessory heavy mineral fractions. Comparably large barite particles commonly occur in minor amounts around 0.25 to 0.35%. Pyrochlore and Ba-pyrochlore are common accessory Nb phases that occur in a fraction between 0.1 to 0.3 % but might reach up to 1.5%. Pyrochlore is commonly observed as euhedral to subhedral crystals, fully liberated or encapsulated by gorceixite, quartz, or apatite. Differing BSE grey-scale values originate from varying Ba-contents that occur in distinct zones or irregular schlieren. Zr-minerals like zirconolite (0.05 to 0.25%) and baddeleyite (0.05 to 1,5%) occur strictly as accessories. The Zr-oxide baddeleyite occurs liberated or intergrown with apatite. Rare

intergrowth occurs with Fe-oxides, quartz, or gorceixite. Zirconolite shows a less distinct affinity of intergrowth with specific mineral phases. Intergrowth was observed similarly with apatite, Fe-oxide minerals, gorceixite, and quartz. Zirconolite commonly contains low concentrations of REE.

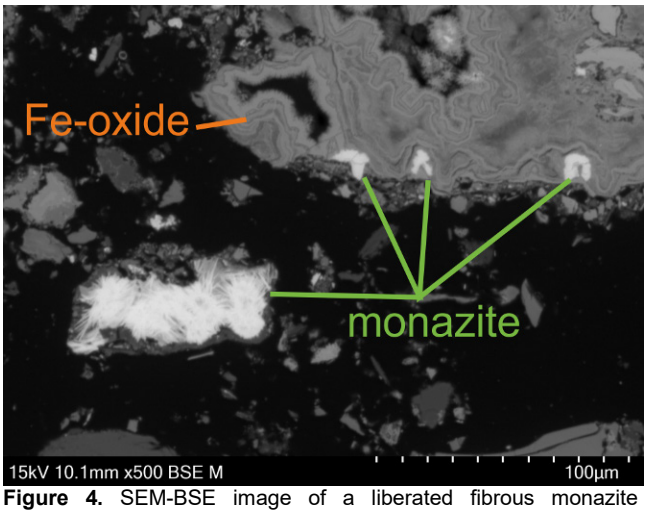

Figure 4. SEM-BSE image of a liberated fibrous monazite aggregate and intergrowth of fine botryoidal monazite with collomorphous Fe-oxide minerals.

Monazite hosts a large portion of the TREO content. Total amounts of this geochemically diverse mineral vary between 0.3 to 0.6 area %. This translates into 0.6 to 1 wt % of potentially accessible REE-mineral content. Rarely, even up to 2 wt % REE-phosphate have been documented. In conjunction with the TREO from geochemically analysed samples, monazite seems to account for 40 to 60 % of the REE content in the samples. Using that relationship could potentially help in predicting further processable quantities of REE. This estimation however is varying for different sample material groups. Monazite particles in the phosphate ore material generally show fine particle sizes with a P-80 between 37 to 43 µm (Fig. 5). The majority (80 wt %) of the particles have a diameter larger than 12 µm (applying a minimum measured particle size of 10 μm^2) A large portion of monazite is intergrown with apatite, quartz, and Fe-oxides. Monazite displays a variety of botryoidal, compact collomorphic, to radial fibrous mineral shapes (Fig. 4). Minute flaky radial monazite was observed as inclusions in apatite and gorceixite.

A high diversity of the mineral shapes might indicate several different monazite generations in the mined ore. Geochemically, monazite also shows a high variability besides the described morphological differences. Elements such as Sr, Ca, and F are commonly detected in monazite particles. So far, no systematic relationship between the trace element content and the specific mineral shape could be established.

Our results from the investigation of the phosphate ore will be put in further context with various process material from the phosphate beneficiation process. These results will hopefully assist to construct a robust and applicable system for the estimation of the recoverable total REE content in ores and process materials.

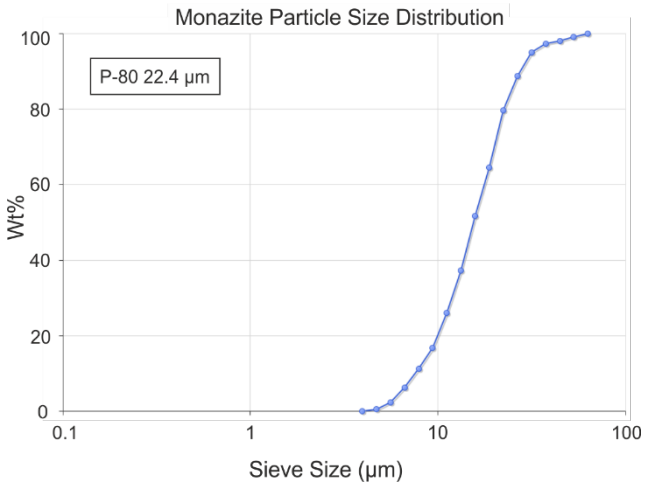

Figure 5. Mineral size distribution of exemplary fine-grained monazite in run of mine stockpile ore.

Acknowledgements

This project is funded by the German Federal Ministry for Education and Research (033R187C). Ceritech AG is greatly acknowledged for transferring know-how and arranging sample logistics.

References

Bardano BMM, Gomes R (2015) Potencial de Aproveitamento de Fontes Secundárias para Terras Raras: Resíduos industriais, vol 86. CETEM Centro De Technologia Mineral

Binnemans K, Jones PT, Blanpain B, van Gerven T, Pontikes Y (2015) Towards zero-waste valorisation of rare-earth-containing industrial process residues: A critical review. J. o, Cleaner Production

Boynton WV (1984) Cosmochemistry of the rare earth elements; meteorite studies. In: Rare earth element geochemistry. Henderson, P. (Editors), Elsevier Sci. Publ. Co., Amsterdam. 63-114.

European Commission (2014) Communication from the commission to the European Parliament, the Council, the European Economic and Social Committee and the Committee of the regions, COM (2014) 297 final, Brussels

Habashi F (1985) The recovery of the lanthanides from phosphate rock. J Chem Tech Biotechnol 35:5–14

Krishnamurthy N, Gupta C (2016) Extractive metallurgy of rare earths, Second edition. CRC Press Taylor & Francis Group, Boca Raton, London, New York

Maak, S, Kamrad, A, Borg, G (2019) Mineralogical and geochemical characteristics of alkaline phosphate ore from a supergene zone in the Catalão Region, Brazil. In this volume

U.S. Geological Survey (2019) Mineral commodity summaries. U.S. Geological Survey, Reston, USA

Pereira L, Birtel S, Möckel R, Michaux B, Silva AC, Gutzmer J (2019) Constraining the Economic Potential of By-Product Recovery by Using a Geometallurgical Approach: The Example of Rare Earth Element Recovery at Catalão I, Brazil. Econ Geol. doi: 10.5382/econgeo.4637

The Cinovec Sn-Li deposit: Challenges for ore processing

Alla Dolgopolova, Reimar Seltmann, Robin Armstrong, Chris Stanley
Natural History Museum, Department of Earth Sciences, London, UK

Jens Andersen, Gavyn Rollinson, Beth Simons
Camborne School of Mines, University of Exeter, UK

Chris Broadbent
Wardell Armstrong International, London, UK

Vitaly Shatov
VSEGEI St.Petersburg, Russia

Abstract. Mineralogical constraints for improving metal recovery at the Cinovec Sn-Li deposit in Czech Republic are discussed. We emphasize the importance of previously neglected mineralogical parameters that could significantly improve recovery of Li as the main commodity and of the most important by-products that include Sn, W, Ta and Nb. This research was performed in the frame of the h2020 FAME project aiming to catalyze the valorization of European tin, tungsten and lithium resources.

1 Introduction

The Cínovec-Zinnwald deposit is located in the eastern Erzgebirge/Krušne Hory area and extends across the Czech and German state border (Fig. 1). Both parts of the deposit are currently being explored by drilling for Sn-Li vein and greisen ores, accompanied by advanced ore processing tests.

Cinovec hosts the largest lithium resource in Europe, and one of the largest undeveloped tin resources in the World. A recently completed Preliminary Feasibility Study indicates that Cinovec has the potential to be the lowest cost hard rock lithium producer in the World (https://www.europeanmet.com/cinovec-lithium-tin-project/).

In our research, aiming to contribute to an increase in by-product recovery, we address some of the petrographic, mineralogical and geochemical criteria that affect ore processing.

2 Geological setting

The Zinnwald-Cínovec granite hosting world-class Sn-W-Li deposits forms an elliptical granite cupola outcropping 1.3 km in N-S direction. The W contact of the intrusion is steep, whereas the S, SE and E contacts plunge with 10 to 30°. The upper part of the intrusion is formed by lithium-albite granite, underlain by medium-grained protolithionite granite at a depth of 730 m beneath Cínovec (Štemprok and Šulcek 1969; Rub et al. 1983). In the cupola, the lithium-albite granite consists of two textural varieties: an older porphyritic granite and a younger medium-grained seriate granite that encloses the relicts of the porphyritic granite. Zinnwaldite is the predominant mica in the lithium-albite granite.

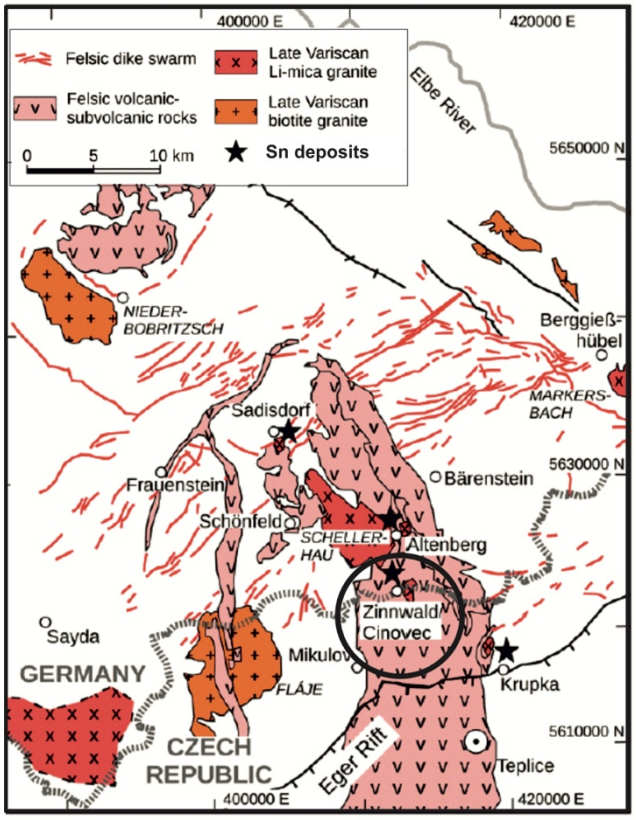

Figure 1. Late- to post-collisional highly evolved granite magmatism in the Erzgebirge, Germany-Czech border area. Asterisks show location of Sn deposits (from Zhang et al. 2017).

3 Mineralogical and petrographic study

The **lithium-albite granites** (synonyms: alkali feldspar granites or Li-F granites) contain on average 0.11 wt.% Li_2O and 4.62 wt.% K_2O. Plagioclase is absent, sodium feldspars are represented by albite with a low (<3 wt.%) anorthite content.

Main accessories are cassiterite, fluorite, topaz, columbite-tantalite in addition to rare bastnaesite, uranpyrochlor, uranmicrolite, strueverite, synchisite (Johan and Johan, 1993; Rub et al., 1998).

The **protolithionite granite** contains on average 0.05

wt.% Li_2O and 5.34 wt.% K_2O.

Main accessories are zircon, columbite, monazite, xenotime and rutile. Apatite is very rare.

The low-grade Li ore is confined to zinnwaldite with substantial Rb and Cs contents. In addition, the ore contains cassiterite, wolframite and scheelite as Sn and W carriers. Apart from this, the Sn and W concentrates contain considerable contents of Nb, Ta, and Sc.

The large petrographic and mineralogical variability of magmatic rocks and their alteration products is shown in figures 2 and 3; with quartz, potassic feldspar, albite, topaz, di- / trioctahedral micas, clays, and accessory minerals having main impact on metal recovery.

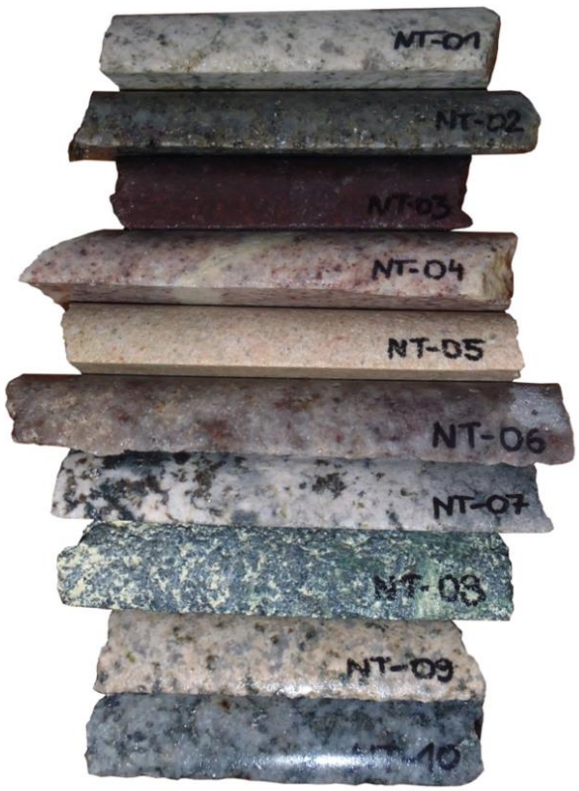

Figure 2. Mineralogical and petrographic variability of granites and greisens from Cínovec drill core (scale: half core sample NT-06 is 10 cm long).

Mica chemistry changes with compositional evolution of their granite hosts and it fingerprints the ore-generating potential of mineralized granitic systems as well as interaction of granite melts with their metamorphic wall-rocks. Furthermore, in highly evolved Li-F granite-ore systems such as Zinnwald-Cinovec, the magmatic-hydrothermal transition processes are characterized by intense "autometasomatic" fluid-rock interaction (Štemprok and Šulcek 1969).

Intrusive pulses and oscillating fluid release control continuous re-equilibration of mineral phases in time and space which explains the mica variability in the mineralized cupola with vertical petrographic zonation and mica zonation itself (Fig. 4).

The three observed genetic mica types include: magmatic-hydrothermal lithium mica (zinnwaldite, protolithionite, etc.), pseudomorph metasomatic replacements (high-Li: lepidolite) and tropomorph (low-Li: muscovite) metasomatic replacements.

The issue of accurate direct in-situ Li determination in micas, traditionally performed by recalculation of Li values from EPMA data using stoichiometry (Breiter et al. 2017, 2019), can be overcome by direct measurement of Li by LA-ICP-MS. The data obtained by the two methods correspond well to each other.

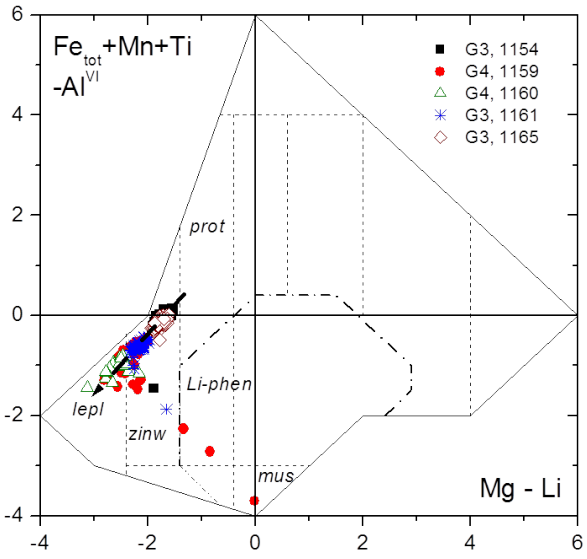

Figure 3. Mineralogical variability and evolution trends of lithium mica from Zinnwald-Cínovec (Fedkin et al. 2001): Li-Phengite - Zinnwaldite - Lepidolite (plot after Tischendorf et al., 1997).

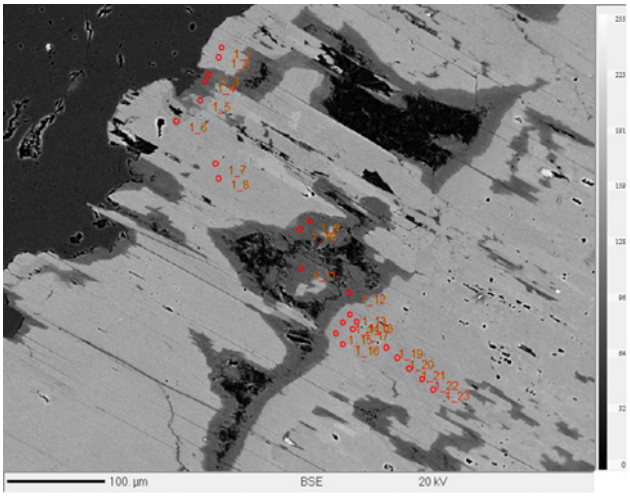

Figure 4. SEM BSE image of zinnwaldite with rims of retrograde muscovite.

4 QEMSCAN study

The QEMSCAN, an automated quantitative mineralogy technique, aids ore characterization for communition. The

QEMSCAN analysis was carried out with the QEMSCAN® 4300 at Camborne School of Mines, University of Exeter (Fig. 5).

The studied ore is dominated by zinnwaldite (76 vol%) with minor clays (9 vol%), topaz (5 vol%) and quartz (4 vol%). Fluorite (1 vol%) partially replaces zinnwaldite, particularly along the cleavage planes of grains. The ore contains clusters of cassiterite (<50 µm, 0.01 vol%), locked primarily within zinnwaldite, less commonly fluorite.

Wolframite, columbite and scheelite are trace phases only (<0.01 vol%). Zircon, monazite, sulphides and uraninite are also trace phases only (<0.01 vol%) (Figs. 6, 7; Table 1).

Figure 5. Visual appearance of thin section in transmitted light (left figure) and QEMSCAN® false colour map (right figure).

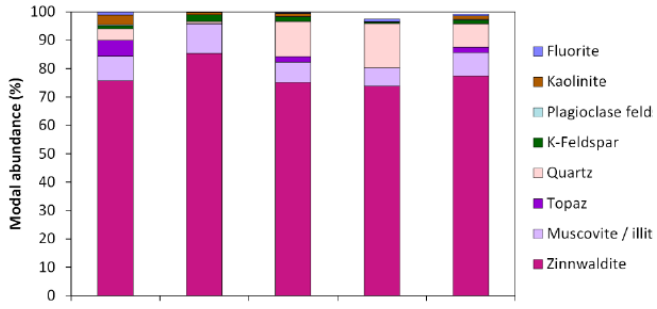

Figure 6. Modal abundances (vol%) for gangue and zinnwaldite.

Table 1. Mineralogical composition (Volume %) and size distribution identified by QEMSCAN (CSM University of Exeter).

Mineralogical composition (vol %)[2]

Zinnwaldite	75.67	Apatite	Tr.
Muscovite / illite*	8.78	Fe-Ox/CO3	Tr.
Topaz	5.51	Uraninite	Tr.
Quartz	4.15	Others	Tr.
Kaolinite	3.35	Galena	Tr.
Fluorite	1.11	Columbite	Tr.
K-Feldspar	0.98	Rutile	Tr.
Plagioclase feldspar	0.39	Scheelite	Tr.
Tourmaline	0.02	Wolframite	Tr.
Calcite	0.01	Bismuthinite	Tr.
Cassiterite	0.01	Sphalerite	Tr.
REE minerals	0.01	Chalcopyrite	n.d.
Chlorite	0.01	Cu arsenides	n.d.
Zircon	Tr.	Cobaltite	n.d.
Pyrite	Tr.		

Size distribution (max | min| mean)[3]

Zinnwaldite	6 mm	10 µm	521 µm
Cassiterite	145 µm	<10 µm	26 µm
Wolframite (Tr.)	-	-	≤15 µm
Scheelite (Tr.)	-	-	32 µm
Columbite (Tr.)	-	-	≤15 µm
REE minerals	120 µm	<10 µm	32 µm

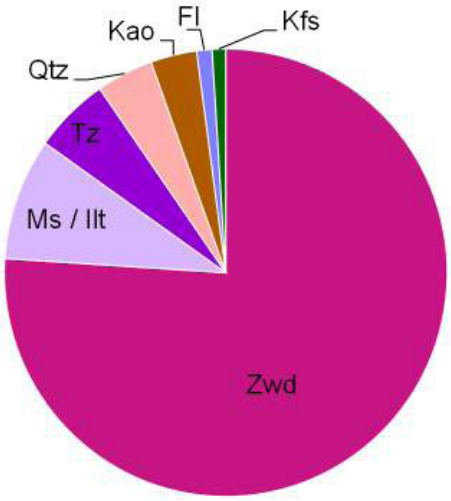

Figure 7. Visual representation of mineralogy (not <0.01 vol%): Gangue (+ zinnwaldite).

5 Optimising ore processing of Li-micas

Identifying key Li-bearing mineral phases has important implications for an optimized ore processing. Samples from the Cinovec deposit show a variety of main Li-bearing mineral phases such as zinnwaldite, muscovite and lepidolite (Fig. 8). Whereas the grain size distribution and density of the various mica phases are rather similar or in a close bandwidth, the magnetic behavior of Fe-Ti rich mica is the most contrasting petrophysical feature suggesting the application of magnet separation to achieve an optimized Li recovery. The magnetic susceptibility contrasts between zinnwaldite (paramagnetic) and lepidolite (diamagnetic) allow their successful separation. Muscovite is a common non-magnetic phase of late (retrograde) alteration, accompanying clayey phases in intergranular space, as zonal ongrowth, in cleavage of instable earlier Li mica or as replacement of tropomorphic alteration.

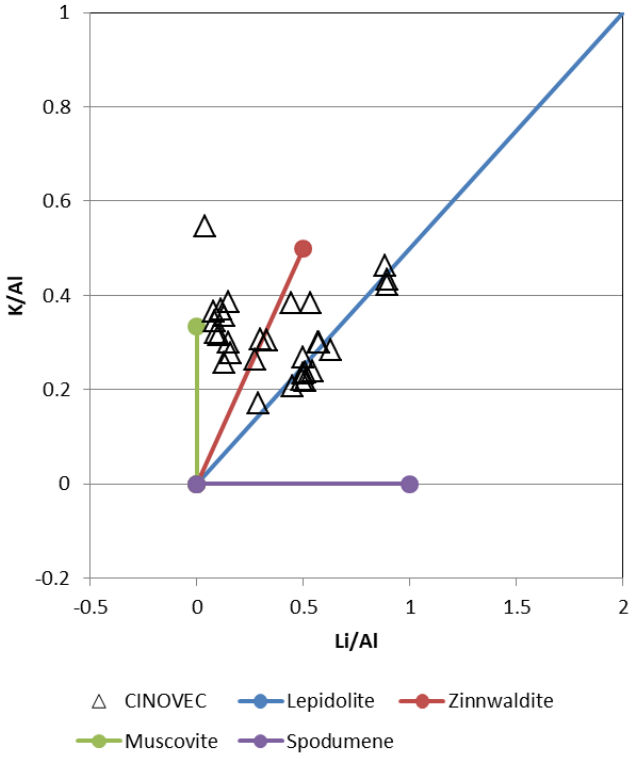

Figure 8. Li/Al vs. K/Ak plot showing main Li-bearing phases at the Cinovec deposit.

6 Key challenges for ore processing

As key challenges for an optimized ore processing the following geological (petrographic, mineralogical, geochemical) constraints have been identified:

- Subhorizontal thin-layered anatomy of ore bodies (sheeted laccolite, alteration zones, flat ore bodies);
- Strong petrographic-mineralogical variability;
- Contrasting magnetic properties of mica phases;
- Variable grain size and strong Li zonation of mica;
- Low-temperature clayey alteration in intergranual space could lead to Li loss in slimes;
- Problematic (or penalty) minerals: topaz – extremely hard and causes excessive wear on crushing and grinding equipment;
- Uraninite and pitchblende are trace radioactive minerals and could impact the final product if not removed.

A previously neglected mineralogical parameter but important for increased by-product recovery are the elevated contents of Nb and Ta in the alkali feldspar granites (outside the Li-Sn cut-off of the greisen ore bodies).

Acknowledgements

The research was co-funded by the EU Horizon 2020 Project "FAME": *Flexible and Mobile Economic Processing Technologies* (grant #641650). The authors acknowledge the contributions of the whole FAME consortium for sample collection and preparation as well as scientific discussions that led to the development of this paper. We greatly appreciate the continuous support and cooperation of Neil Meadows, Pavel Reichl and Vojtek Sesulka of European Metals Holdings Ltd. / GEOMET, UK / Czech Republic.

References

Breiter K, Ďurišová J, Hrstka T, Korbelová Z et al. 2017 Assessment of magmatic vs. metasomatic processes in rare-metal granites: A case study of the Cínovec/Zinnwald Sn-W-Li deposit, Central Europe. Lithos 292-293: 198-217.

Breiter K, Hložková M, Korbelová Z, Vašinová Galiová M 2019 Diversity of lithium mica compositions in mineralized granite–greisen system: Cínovec Li-Sn-W deposit, Erzgebirge.Ore Geology Reviews 106: 12-27.

Fedkin A, Seltmann R, Förster HJ 2001 Li-bearing micas as the fractionation indicator of tin granites: The Sadisdorf-Schellerhau granite suite, Eastern Erzgebirge. Mineral Deposits at the Beginning of the 21st Century, Piestrzynski et al. (eds). Swets & Zeitlinger Publishers Lisse: 409-412.

Johan V, Johan Z 1993 Accessory minerals of the Cínovec (Zinnwald) granite cupola, Czech Republic, part 1. Nb-, Ta-, and Ti-bearing oxides. Mineral. Petrol. 49: 1-21.

Rub MG, Pavlov VA, Rub AK, Štemprok M, Drábek M, Drábková E 1983 Elements of vertical zoning in the Cinovec massif of lithium fluorine granites (Czechoslovakia). In: Correlation of magmatic rocks of Czechoslovakia and some districts of the USSR Izd. Nauka, 108-137, Moskva (in Russian).

Rub AK, Štemprok M, Rub MG 1998 Tantalum mineralization in the apical part of the Cínovec (Zinnwald) granite stock. Mineral. Petrol. 63: 199-222.

Štemprok M, Šulcek Z 1969 Geochemical profile through an ore-bearing lithium granite. Econ. Geol. 64: 392-404.

Tischendorf G, Gottesmann B, Förster H-J and Trumbull RB 1997 On Li-bearing micas: estimating Li from electron microprobe analysis and an improved diagram for graphical representation. Mineralogical Magazine, 61, 809-834.

Zhang R, Lehmann B, Seltmann R, Sun W, Li C 2017 Cassiterite U-Pb geochronology constrains magmatic-hydrothermal evolution in complex evolved granite systems: The classic Erzgebirge tin province (Saxony and Bohemia). Geology 45(12): 1095–1098.

Mineral processing and mineralogical characterization of pre-concentrates from the Rondônia Tin Province, Brazil

Simon Goldmann, Herwig Marbler
Federal Institute for Geosciences and Natural Resources (BGR)

Frank Haubrich
G.E.O.S. Ingenieurgesellschaft mbH

Tiago Buch
Companhia de Pesquisa de Recursos Minerais (CPRM) - Geological Survey of Brazil

Abstract. Processing tests are performed on pre-concentrates (about 60 kg each) from the Cachoeirinha and Bom Futuro mines to improve the recovery of cassiterite and columbite. The processing steps for the pre-concentrates include sample splitting, sieving, density and magnetic separation. The processing steps are accompanied by mineralogical characterization of the concentrates using scanning electron microscopy with Mineral Liberation Analysis software and geochemical analyses by handheld X-ray fluorescence. After sieving, both pre-concentrates can be successfully upgraded by density and magnetic separation to saleable concentrates at high grades and recovery.

1 Introduction

The present study is part of a cooperation project between the Federal Institute for Geosciences and Natural Resources (BGR), which is the Geological Survey of Germany, with Companhia de Pesquisa de Recursos Minerais (CPRM), the Geological Survey of Brazil. The aim of this study is the improvement of processing methods to optimize the recovery of cassiterite (major ore for Sn), columbite (major ore for Nb and Ta) and subordinate byproducts (e.g. zircon) to increase the economic output of marketable mineral concentrates from the Brazilian state of Rondônia. During a first reconnaissance study, geochemical analysis of pre-concentrates and tailings identified that quite a considerable amount of ore minerals is lost into the tailings during processing. This is the main reason for the processing tests in order to check if recovery could be improved. Here we show the results on pre-concentrate samples from the Cachoeirinha and Bom Futuro mines.

2 Geological setting

The Rondônia Tin Province is located in the southwestern part of the Amazonian Craton and is composed of Paleo- to Mesoproterozoic metamorphic rocks, which were intruded by several events of Rapakivi magmatism (A-type granites) between 1600 and 970 Ma (Fig. 1; Bettencourt et al. 1999).

The Sn-Ta-Nb deposits are closely associated with late-stage peraluminous, partly porphyritic alkali-feldspar granites of the Younger Granites of Rondônia suite (998-974 Ma; Bettencourt et al. 1999). The primary mineralization styles are greisen bodies, quartz veins, and pegmatites. However, the exploited ores are mainly derived from the secondary alluvial and colluvial placer deposits, but also former tailings are re-processed. In Bom Futuro, 10 to 15 % of the production is also from primary ores.

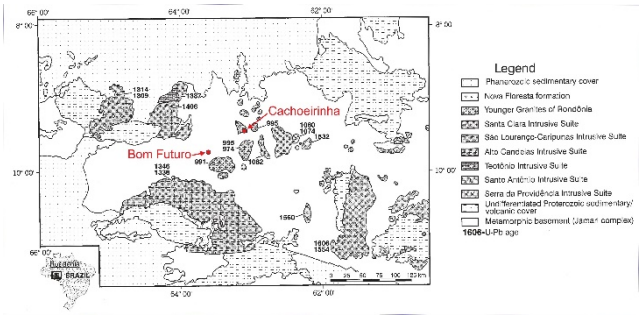

Figure 1. Geological map of the Rondônia Tin Province showing location of the respective sample sites. Insert shows the position of the map within Brazil (Bettencourt et al. 1999)

3 Materials and methods

3.1 Samples

Jigs are the initial processing step in the Cachoeirinha and Bom Futuro mines and bulk samples (about 60 kg each) are taken from the 2nd chamber of the jigs as starting material for further processing test work. The best quality is produced in the 1st chamber, but these concentrates are not treated for this study. Polished sections are prepared from these initial bulk samples (after sample splitting) and also from single processing steps during the test work.

3.2 Instrumental

Mineralogical parameters (like composition, grain size distributing and intergrowths) are identified using a FEI Quanta 650F scanning electron microscope with two Bruker energy-dispersive X-ray spectrometers (EDX) and Mineral Liberation Analysis (MLA) software. The MLA software uses the EDX system combined with

backscattered electron imaging to automatically identify mineral phases in ore concentrates by comparison of the X-ray spectra with those from standards stored in a database (Fandrich et al. 2007).

Geochemical analyses were performed using a Bruker S1 TITAN handheld X-ray fluorescence (XRF) on an aliquot of about 10 g of ground (<100 µm) sample for each processing step. The accuracy of the handheld XRF analyses are sufficient to monitor the enrichment or depletion of relevant elements along the processing path.

3.3 Mineral processing

The general processing procedure applied for the pre-concentrates includes sample splitting, sieving, density and magnetic separation. Subsamples of 1 kg from each pre-concentrate are sieved in 100 µm steps in order to determine which particle size fractions contain the largest amount of valuable material also in relation to mass of the respective fraction.

The enrichment of the heavy ore minerals takes place by density separation using a shaking table with a stroke length of 16 mm at 220 strokes per minute. For this purpose, the remaining bulk pre-concentrates are sieved into four particle size fractions with the following ranges: 63-250, 250-500, 500-710 and 710-2000 µm.

Subsequently, all heavy fractions (HF1 and HF2) from the shaking table are split into para- and diamagnetic fractions (the ferromagnetic fraction is very low) using a magnetic belt separator with a permanent magnet of fixed field strength of 1.1 Tesla.

4 Results and discussion

The pre-concentrate from Cachoeirinha (Fig. 2) is dominated by quartz and topaz, but also contains relatively high concentrations of cassiterite (~5 area%) as well as columbite (~2 area%). Cassiterite is present in high concentrations distributed over all particle sizes. Evaluated MLA data revealed that about 92 % of cassiterite is liberated. This is favorable for processing, because cassiterite is largely present as free grains and only a few grains are intergrown with other mineral phases. Especially in the small particle sizes, SnO_2 (representing cassiterite) is enriched up to 30 wt% and Nb_2O_5 + Ta_2O_5 (representing columbite) up to 15 wt% (Fig. 3). The highest concentrations of up to 5 wt% ZrO_2 (representing zircon) are in the <200 µm particle sizes. In terms of mass, the highest yield of SnO_2 (40 wt%) is in the coarse fraction >800 µm (Fig. 3), whereas Nb_2O_5 and Ta_2O_5 are distributed over the entire particle size range. The highest concentrations of ZrO_2 are only in the 100-200 µm fraction (Fig. 3).

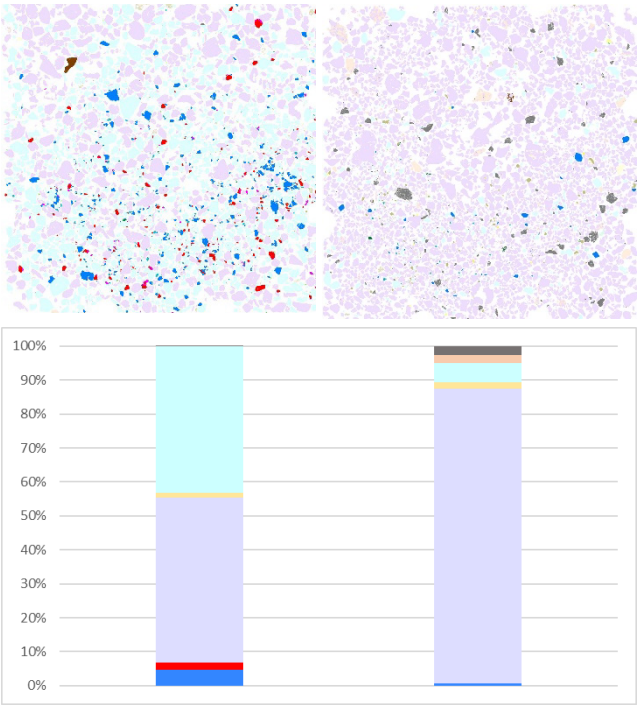

Figure 2. Classified MLA image of pre-concentrates (jig, 2nd chamber) from Cachoeirinha (left) and Bom Futuro (right) and their respective modal mineralogy (blue: cassiterite, red: columbite, violet: quartz, turquoise: topaz, grey: K feldspar, apricot: goethite, yellow: others)

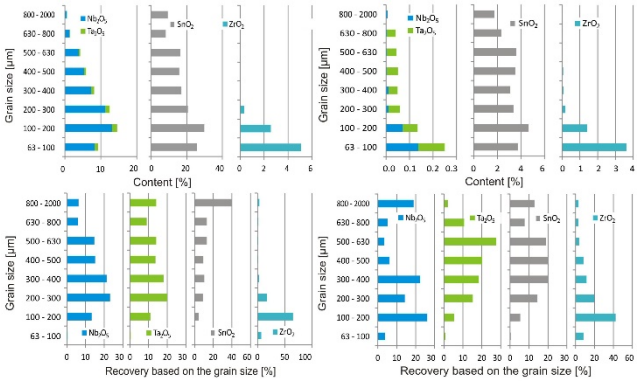

Figure 3. Element content (upper half) and recovery (lower half) dependent on grain size fraction of pre-concentrate from Cachoeirinha (left-hand side) and Bom Futuro (right-hand side)

Quartz is the major phase in the pre-concentrate from Bom Futuro, with minor topaz, goethite and potassium feldspar. Compared to Cachoeirinha, cassiterite is present in lower amounts (~0.6 area%) and columbite is lacking (Fig. 2). Cassiterite is highly liberated up to 97 %. The tin content ranges from 2 to 4 wt% SnO_2 and is rather uniformly distributed over the entire particle size range (Fig. 3). The highest concentrations of Nb_2O_5, Ta_2O_5 and ZrO_2 are in the small particle size ranges <200 µm, but are negligible in terms of mass. The largest proportions of SnO_2, Nb_2O_5 and Ta_2O_5 are >100 µm over the entire particle size range. However, high SnO_2 contents of 1 wt% are also in the >2 mm fraction, which represents about 18 % of total mass of the bulk sample.

4.1 Density separation

During density separation using a shaking table on the pre-concentrate from Cachoeirinha, cassiterite and columbite are almost completely recovered (recovery of >95 %) into the two heavy fractions (HF1 and HF2) and are nearly absent in the middlings (MD) and light fraction (LF). This applies to all four grain size fractions (Fig. 4). The highest mass of HF1 and HF2 is obtained from the 63-200 µm grain size fraction. Due to its small grain size of <200 µm, zircon is concentrated in the 63-250 µm grain size fraction (7.5 wt% ZrO_2) and has highest recovery in HF2 followed by HF1.

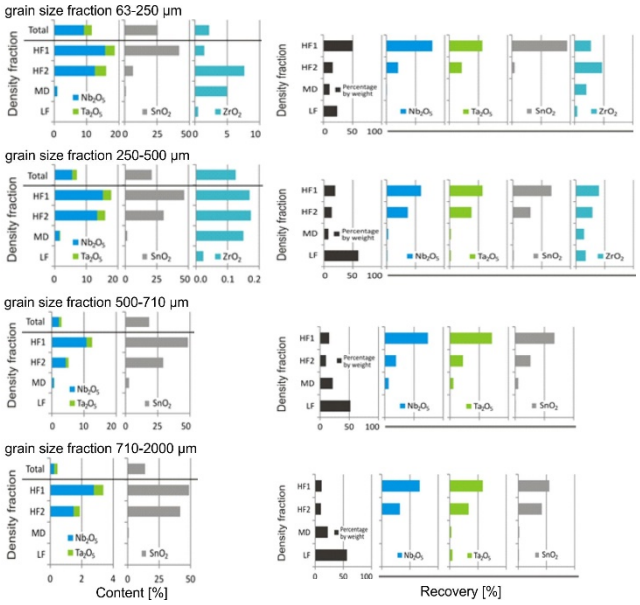

Figure 4. Element content (left) and element recovery (right) for heavy fractions (HF1 and HF2), middlings (MD) and light fraction (LF) from density separation for the different grain size fractions from Cachoeirinha. Top line shows the initial contents of the element oxides for each grain size fraction.

For Bom Futuro, cassiterite is also effectively concentrated especially into the heavy fractions (HF1 and HF2) for all four grain size fractions at >95 % recovery (Fig. 5). Both are almost absent in the middlings (MD) and light fraction (LF). The amount of Nb_2O_5 + Ta_2O_5 is significantly less compared to Cachoerinha and is not present as single columbite grains. Zircon also plays a role in the 63-250 µm grain size fraction and has highest recovery in HF1.

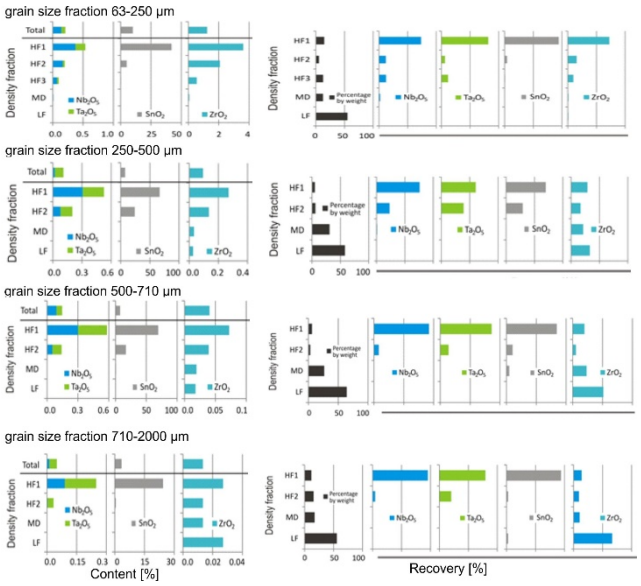

Figure 5. Element content (left) and element recovery (right) for heavy fractions (HF1 and HF2, HF3 just for 63-250 µm fraction), middlings (MD) and light fraction (LF) from density separation for grain size fractions from Bom Futuro. Top line shows the initial contents of the element oxides for each grain size fraction.

4.2 Magnetic separation

The heavy fractions from Cachoerinha contain cassiterite, but also columbite. Both phases can be separated effectively by magnetic separation as cassiterite goes into the diamagnetic fraction, whereas columbite is concentrated in the paramagnetic fraction. In all diamagnetic fractions of HF1 and HF2, high SnO_2 concentrations are achieved with high recoveries of >80%. Overall, only a small amount of SnO_2 entered the paramagnetic fraction, which is possibly due to Fe-rich cassiterite, or cassiterite inclusions in columbite. Columbite was strongly enriched in the paramagnetic fraction. Part of the Nb_2O_5 + Ta_2O_5 were also transferred into the diamagnetic fraction because the cassiterite contains Nb and Ta, either as columbite inclusions, or incorporated as trace elements in the crystal lattice.

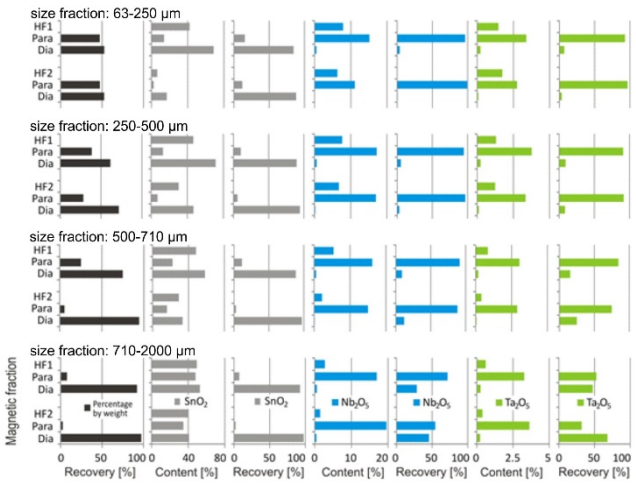

Figure 6. Concentrations and recovery rates in magnetic fractions for different grain size ranges from Cachoeirinha

For heavy fractions from Bom Futuro, cassiterite is recovered at high grades in all diamagnetic fractions, but some cassiterite is lost into the paramagnetic fraction. However, there is no significant enrichment in concentration compared to the heavy fractions from the shaking table. Individual columbite grains are not enriched.

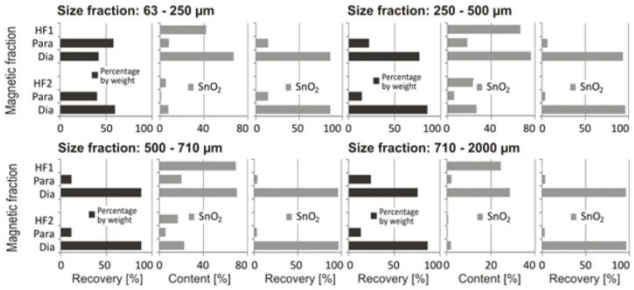

Figure 7. Concentrations and recovery rates in magnetic fractions for different grain size ranges from Bom Futuro

5 Conclusions

The valuable minerals in both pre-concentrates are almost completely liberated and can be successfully concentrated by a combination of density and magnetic separation.

The heavy minerals of interest in the bulk sample from Cachoeirinha are cassiterite, columbite, and zircon. Cassiterite and columbite can be enriched by density separation. Zircon is only enriched in the <200 µm grain size range. To achieve higher recovery for cassiterite and columbite, the HF1 and HF2 fractions should be further processed together. By magnetic separation, cassiterite and columbite can be separated effectively; columbite entering the paramagnetic fraction and cassiterite in the diamagnetic fraction. In the diamagnetic fraction, small amounts of Nb and Ta are present as trace elements or intergrowths in cassiterite. This Nb and Ta content in the cassiterite had to be rated as a loss and are transferred into the slag during tin smelting. However, the slags may be significantly enriched in Nb_2O_5 + Ta_2O_5 and can be considered as an additional raw material.

The valuable mineral at Bom Futuro is cassiterite. As the >2 mm portion contains up to 1 wt% SnO_2, the coarse fraction should be ground to <200 µm to recover this SnO_2 content. Subsequently, an enrichment of the cassiterite via the shaking table is possible. Magnetic separation (if at all) should take place at field strengths lower than 1.1 Tesla to avoid losses of cassiterite into the paramagnetic fraction. No Nb-Ta concentrate could be produced as the initial concentrations are too low and do not occur as individual minerals like columbite, but are present as trace elements within the lattice of other mineral phases.

Acknowledgements

We gratefully acknowledge the preparation of excellent polished sections by Don Henry and Andreas Heiner at BGR. We also would like to thank the companies METALMIG and COOPERSANTA for access to their mine sites, permission to take samples and logistical support.

References

Fandrich R, Gu Y, Burrows D, Moeller K (2007) Modern SEM-based mineral liberation analysis. Int J Miner Process 84:310-320.

Bettencourt JS, Tosdal RM, Leite Jr. WB, Payolla BL (1999) Mesoproterozoic rapakivi granites of the Rondônia Tin Province, southwestern border of the Amazonian craton, Brazil: I. Reconnaissance U-Pb geochronology and regional implications. Precambrian Res 95:41-67

Processing waste of feldspar raw material as source of valuable metals: pre-full-scale laboratory study and search for optimum separation flowchart

Tomáš Vrbický, Richard Přikryl
Institute of Geochemistry, Mineralogy and Mineral Resources, Faculty of Science, Charles University in Prague, Czech Republic

Abstract. Leucogranites that are exploited at Krásno – Vysoký kámen deposit (Krásno ore district, Slavkov crystalline unit, western part of the Bohemian Massif, Czech Republic) are used as a feldspar raw material. These rocks are product of hydrothermal metasomatic alteration of Variscan granites. As the exploited material is utilized mainly by ceramic and/or glass industries, the content of harmful colourants presents a critical issue. Laboratory and small-scale processing trials by combination of magnetic and gravity separation aimed in reduction of the content of harmful phases. Mineralogical and chemical analyses of the obtained waste have shown that it is enriched in phases with high concentration of elements such as Li, Nb, and/or Ta which are considered as critical raw materials in EU.

1 Introduction

Feldspar-rich leucogranite formed by metasomatic / hydrothermal alteration of original granite makes one of the largest resources of feldspar raw material in the Czech Republic. Studied material consists mainly of albite and quartz accompanied with minor amounts of minor / accessory phases (Fe-, Mn-, Ti-rich phases partially with complex mineralogical binding with Nb-Ta, Li-micas, and apatite). The latest phases represent the major harmful components because their potential to cause colour changes in the final product.

As the exploited feldspar raw material is primarily used as one of the major components in the ceramic and glass industry, its quality is carefully controlled; this concerns specifically content of undesirable pigmentation components.

Due to overall mineralogy/geochemistry of the exploited deposit, part of excavated material is processed by newly installed dry magnetic separation. This processing results in generation of several tons of magnetic separate which is currently deposited nearby the quarry and can be generally viewed as a “waste” or currently non-usable by-product. However, extreme enrichment in phases such as Li-micas, and/or Nb-Ta-rich Ti-oxides lead authors to the idea on potential re-processing of the by-product and separation of individual phases which contain elements being currently classified as “critical raw materials” by EU and other countries.

The previous studies of the authors focused mainly on detailed mineralogy of the exploited raw material and on preliminary laboratory scale trials aiming to evaluate individual processing methods for separation of individual phases. Considering the technical, economical, and ecological feasibility of available separation methods, combination of dry magnetic separation and air gravity concentrating table appeared to be very effective. Therefore, the recent study presents a step further: pre-industrial scale separation trials by using several tens of kg of by-product material. This step is a necessary for formulation of real, industrial-scale experiment which will use several tons of material and will be used as a basis for adoption of processing scheme in real feldspar raw material processing flowchart.

2 Geological setting

The main extracted raw material is alkaline - feldspar granite (albitic granite) which belonging to Krásno ore district situated in western part of Bohemian Massif (Czech Republic) (Pácal and Pavlu 1979). This feldspar deposit makes part of the granitic and locally greisenized stock Vysoký Kámen. (Sejkora et al. 2006). The deposit occupies an area of approximately 400 x 600 m in widht and reaches a thickness to 190 m in depth (Hron and Kottnauer 2007). The exploited raw material is composed of prevalent feldspar minerals, specifically albite (Nosek 1997).

Granites are white to slightly pink, with an albite content of 30-50% and a K-feldspar content of 20-30%. In the case of feldspatite, feldspars form more than 75% of the mass.

Another important mineral is quartz (20 - 40%), which together with the feldspar is the main rock-forming minerals (Jarchovský 2006). Most rocks also contain mica, which are marked as Li - muscovite, cinvaldit or polylithionite. The distribution of mica is very variable in the bearing area. Top quality parts contain mica only accessory, whereas in the edge parts of mine, it is possible to find large mica crystals up to several centimeters. Another mineral, whose representation is variable, is topaz. In some rocks topaz has not been found, while some samples have a content of about 10% (Hron and Kottnauer 2007). Another important mineral is apatite, whose representation is very variable, as in the previous case. The locality is mineralogically quite rich and contains many accessory minerals.

There are up to 15 cm large greenish berylliums. In quartz veins there are hemispherical aggregates of

radially arranged hematite crystals. Other minerals found include wolframite, bismuth, beryl, bertrandite, molybdenite or scheelite. (Beran 1999; Sejkora et al. 2006). In the area of the quarry was also discovered hollandite reaching several centimeters (Pauliš et al. 2014). In a cracks can be found significantly yellow-green (meta)autunite and autunite. (Pauliš 1990). In addition to these there are also younger alteration products such as russelite and clay minerals (Beran 1999). There are also muscovite, sericite and rutile (Jarchovský 2006). The site is mineralogically rich and there are supposed to be other minerals, especially phosphates.

3 Separation methods and results

According to the results of previous separation trials on laboratory scale done by the author, the small-scale separation experiments focused finding the optimum flow chart of separation techniques that would be further tested on full-scale. The general aims of these experiments were twofold: (1) increase of purity of feldspar raw material (i.e. removal of the phases bearing colourants – specifically Fe- and Ti-rich phases), and (2) effective separation of phases being present in the "waste" from previous step (i.e. trial to convert "waste" into the valuable byproduct(s)).
Based on the results of previous laboratory study, the combination of dry magnetic separation and air gravity concentrating table proved to be very effective.

The combined gravity and magnetic separations were used to divide the material to individual components. Specifically, dry magnetic separation, wet shaking table and high density liquid was used. This process resulted in several fractions of relatively pure concentrates.

The main obtained concentrates are (Fig.1):
1 – Micas concentrate
2 – Apatite concentrate
3 – Nb-Ta rich concentrate
4 – Fe-Mn rich concentrate

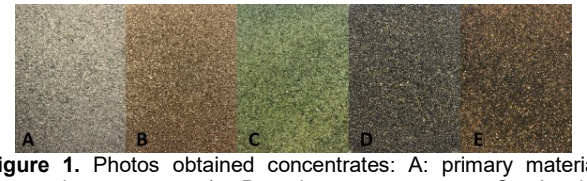

Figure 1. Photos obtained concentrates: A: primary material (magnetic concentrate), B: micas concentrate, C: Apatite concentrate, D: Nb-Ta-rich concentrate, E: Fe-Mn-rich concentrate.

Small-scale separation experiment focused on selection of optimal devices/processes that can be used for further processing (i.e. separation of individual components) of "waste" material generated during feldspar raw material processing. The specific interest was on separation of Li-rich micas and Nb-Ta minerals. About 50 kg of input material was employed for experiments.

The effectiveness of applied separation techniques was controlled though chemical analyses of the initial input material and the end-products of the separation process by using XRF and SEM-EDS. For selected samples, content of specific light elements (e.g., of Li) was determined by wet silicate analysis. Control measurements of phase composition from powder XRD was done as well.

4 Discussion

4.1 Composition of magnetic concentrate

The studied material consists of several major minerals, which can be divided into almost pure fractions.

Micas are mostly represented by Li-micas with variable Fe content (Fig. 2). Some of mica are partially eroded and transformed to clay minerals.

Apatite occurs as microcrystalline aggregates, fill in cracks and also as zonal monocrystals.

Nb-Ta rich concentrate consist mainly of Nb-Ta rich rutile grains (Fig 3.) & less extant grains of Nb-Ta minerals (ferocolumbite).

Fe-Mn oxides are represented mostly by hematite and hollandite. Which can make crystals even a few centimeters.

Last mineral that is in the material more abundant is topaz. Other minerals are only accessory.

4.2 Small-scale separation

Li mica separation
To obtain Li-rich micas concentrate, dry electro-magnetic separation appeared to be very effective. By using input material with 0.2 / 0.8 mm granulometry, it was possible to obtain relatively pure mica concentrate exhibiting 2.1 wt.% of LiO_2 in average.

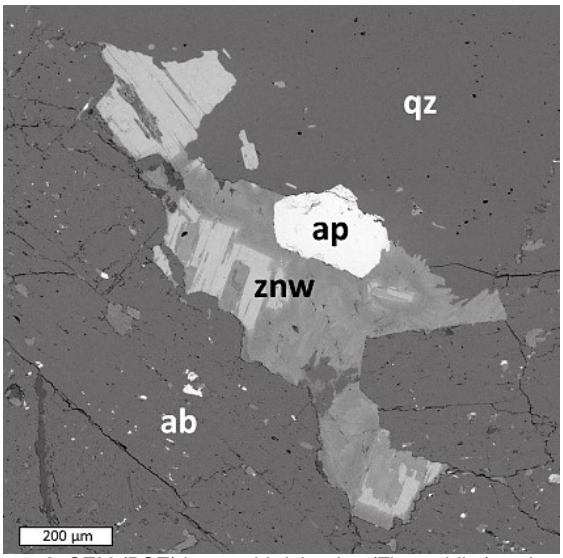

Figure 2. SEM (BSE) image: Li-rich mica (Zinnwaldite) grain with overgrown apatite.

Nb-Ta rich mineral separation
To obtain Nb-Ta rich phases, the wet gravity and dry gravity methods have been tested. Both of these methods were very effective and can be used to obtain

a concentrate containing first percents of Nb_2O_5. Air gravity concentration table appears to be proper and very effective method for heavy minerals concentrating.

Due to grain size of constituent minerals, the processing appeared to be most effective for input material having granulometry of 0.2/0.5 mm. Wet shaking table can also be employed for material with finer granulometry, but its use in operation would be much more complicated than in the optimum grain size distribution. Concerning the coarser input material (grain size above 0.5 mm), the separation of Li-, Nb-Ta-bearing phases is impossible as these phases are not liberated from the quartz-feldspar matrix. The effective separation is thus controlled by the optimum granulometry of the input material allowing for liberation of individual phases during crushing.

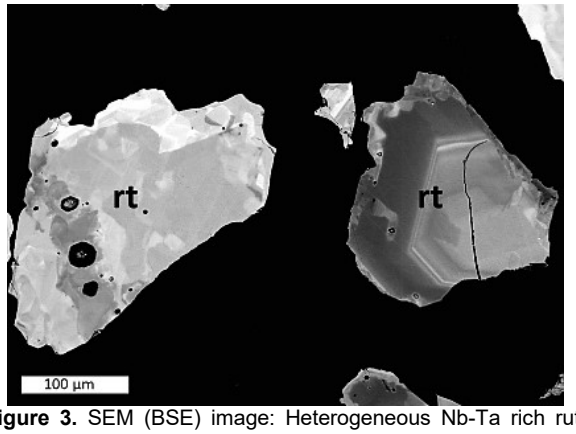

Figure 3. SEM (BSE) image: Heterogeneous Nb-Ta rich rutile grains.

5 Conclusions

The studied material consists of several major minerals, which can be divided into almost pure fractions, such as Li-micas, apatite and Nb-Ta minerals. Combination of dry magnetic separation and air gravity concentration table seems to be a very effective way on how to separate Nb-Ta-rich phases and Li-mica from material which is generated in feldspar raw material processing.

Acknowledgements

The financial support to this study from the Grant Agency of Charles University in Prague (Project No. GAUK 1352218) is highly acknowledged. We are also grateful for logistics, additional financial support and access to analytical techniques (XRF) and analytical support KMK GRANIT company.

References

Beran, P. (1999) Nerosty cíno-wolframových ložisek Slavkovského lesa. Sokolov museum and library.

Hron, M., Kottnauer, R. Punčochář, M. (2007) Krásno - ložiskový průzkum 2006, etapa průzkumu: podrobná, No. 2700981. Final report. Unpublished report.

Jarchovský, T. (2006) The nature and genesis of greisen stocks at Krásno, Slavkovský les - western Bohemia, Czech Republic. Journal of the Czech Geological Society, 51: 201–216.

Nosek, P. (1997) Přehodnocení ložiska Krásno - Vysoký Kámen. Surovina: živcové suroviny. Gekon, s.r.o., Praha 9. Unpublished report.

Pácal, Z., Pavlů, D. (1979) Závěrečná zpráva dílčího úkolu 4/09-4 za léta 1976 - 1979 živcové suroviny - Krásno, Ústřední ústav geologický, Praha. Unpublished report.

Pauliš, P. (1990): Autunit z Vysokého kamene (Krásno) u Horního Slavkova. Casopis pro mineralogii a geologii, 35, 1, 105–106.

Pauliš, P., et al. (2014): Hollandit z Vysokého Kamene u Krásna. Minerál, 6, 22:530–532.

Sejkora, J., et al. (2006): New data on mineralogy of the Vysoký Kámen deposits near Krásno, Slavkovský les area, Czech Republic. Journal of the Czech Geological Society, 51(1-2):43–55.

Graphite raw material in the Bohemian Massif - processing for future mining

Michal Poňavič, Anna Vymazalová, Bohdan Kříbek, František Pticen, Jan Jelínek
Czech Geological Survey, Prague, Czech Republic

Abstract. Critical raw materials in the Czech Republic have been studied under the frame of the project Competence Centre for Effective and Ecological Mining of Mineral Resources. The aim of this study was the improvement of graphite processing of the material samples from the Český Krumlov-Městský vrch deposit using the delamination of graphite-mica composite from the concentrate after the first flotation process. In order to delaminate the graphite-mica composite of the fraction grain size 100–150 μm, before the second flotation process, the destructive methods of ultrasound (US), frost cycles and repeated heating were applied. The process of destroying was tested at various US frequencies, at different intensities and times of processing (2 to 30 minutes). The delamination based on triple repeated frost cycles was performed at -18 ºC and +24ºC. Delamination based on repeated heating up to 150ºC was conducted in two cycles. The most efficient improvement of ore processing has been shown by applying the method of delamination of graphite-mica composite after the second flotation.

1 Introduction

This study has been performed under the project Competence Centre for Effective and Ecological Mining of Raw Materials, funded by the Technology Agency of the Czech Republic (TA ČR) under the leadership of the Technical University of Ostrava (TUO). The aim of the project is to study critical raw materials (CRM) of the European Union (EU), assess the suitable resources of CRM in the Czech Republic and propose a possible efficient and environment-friendly way of their mining and processing.

One of the most important topics of the project is the detailed study of Czech graphite deposits. Graphite was declared to be a critical raw material due to its importance in crucial industries such as steel, lithium-ion batteries, and nuclear reactors. Lithium-ion batteries, widely used in cell phones, power tools and notebook computers, contain almost twenty times more graphite than lithium. Graphite being an essential ingredient in the production of the lithium-ion batteries that power the electrical and hybrid vehicles is forecasted to increase the demand in the future. Over 70 % of world production of natural graphite powders holds China, followed by Latin America, EU production of natural graphite powder is less than 1 %. The Czech Republic does not produce natural graphite domestically and is completely dependent on imports for graphite supply.

Since 2008 there is no mining of graphite in the Czech Republic due to economic reasons but also due to difficulties in processing of the material. However, in the recent years there is an increased interest in reopening of graphite mining. All graphite deposits in the Czech Republic belong to the metamorphogenic type. They originated during the regional metamorphism of clayey sandy sediments rich in organic matter, which is also indicated by higher concentrations of S, P, V and Sr (Franěk et al. 2011). The deposits are located within the Bohemian Massif in two regions: South Bohemian Moldanubicum, and in the Moravicum and Silesicum (Fig. 1). South Bohemian graphitic rocks have a character of graphitic gneisses and carbonates. Deposits in the Moravian-Silesian region occur in an area affected by lower grade metamorphism.

The most important deposits (**Český Krumlov-Městský Vrch** and others) occur in the Moldanubicum, particularly in the so-called Varied Group of Českyý Krumlov.

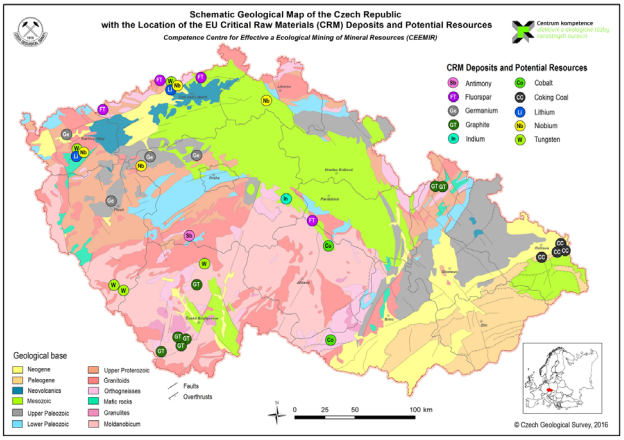

Figure 1. Schematic geological map of the Czech Republic, with the location of the EU CRM deposits and potential resources.

2 Samples and methods

The graphite deposit Český Krumlov-Městský vrch occurs in the central part of the Varied group of Český Krumlov, in the South Bohemian Moldanubicum region.

The deposit is hosted by graphitic paragneiss with a content of graphitic carbon from 8 to 30%. The material also contains blanched biotite, less common muscovite, sericitized and kaolinized feldspars, sillimanite, cordierite and apatite; pyrrhotite and pyrite are also very common, mostly in the form of sulphide impregnations (Tichý 2002). The raw material is formed by crystalline graphite of the size of flake from 0,001–0,5 mm. The deposit is comprised from five ore bodies; their geological structure is very complex (Fig. 2).

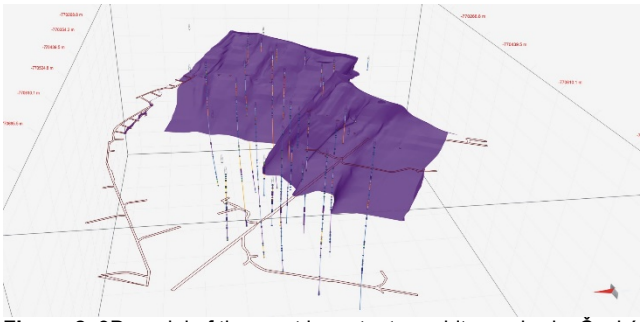

Figure 2. 3D model of the most important graphite ore body, Český Krumlov-Městský vrch deposit, after Jelínek et al. (in print).

We have collected a large volume of samples of graphitic raw material for the further technological tests (Fig. 3).

Figure 3. Macroscopic sample of graphite ore, underground mine, Český Krumlov - Městský vrch deposit.

The processing tests were performed at the TUO. The results of flotation tests have shown the low quality of primary flotation concentrate that proved a content of inner dust and low purity of graphitic flakes. The flakes of graphite are very often epitaxially grown on plates of biotite or white mica (Fig. 4). This, during the crushing and milling of the material, causes the formation of a graphitic composite. Therefore, the full process of flotation processing becomes impeded.

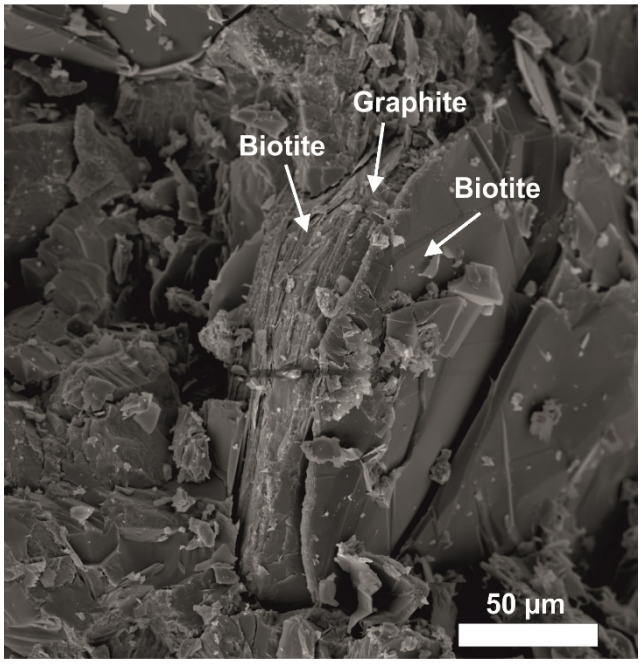

Figure 4. Natural flake of graphite showing fine layers of biotite and graphite, SEM image.

3 Results

The aim, at the Czech Geological Survey, was the improvement of graphite processing of the material samples from the Český Krumlov-Městský vrch deposit using the delamination of graphite-mica composite (Fig. 4) from the concentrate after first flotation process, performed at the TUO. The processing tests were performed at dry conditions after the crushing of graphite in jaw crusher and in oscillatory agate mill. Ultra-fine fraction below 100 µm was separated in air screener ASP HOSOKAWA-ALPINE up level of 40 µm and consequently chemical analyses were performed complemented by a magnetic separation of original milled rock of a fraction 40–100 µm. The Table 1. shows the analyses of selected elements for graphite contaminated by Fe sulphides with a low pH 4. Application of magnetic separation significantly improved to lower the content of sulphides (see Table 1).

In order to delaminate the graphite-mica composite of the fraction grain size 100–150 µm, before the second flotation process, the **destroying methods of ultrasound** (US), **frost cycles and repeated heating** were applied. The process of destroying was tested at various US frequencies from 20 to 40 kHz at different intensities and times of processing (2, 3, 5, 20 and 30 minutes).

Table 1 Chemical analyses of selected elements in raw graphite, non-magnetic fraction (non-mag), after magnetic separation (mag) and after the first floatation of non-magnetic part of graphite.

Graphite	**Original**	Non-mag	Mag	Flotation concentrate Non-mag	0-100 µm	40-100 µm	0-40 µm	**40-100 µm**	40-100 µm
								Non-mag	Mag
Fe	**7.03**	**3.40**	**8.45**	**3.19**	**7.69**	**4.84**	**9.53**	**3.26**	**5.70**
Ti	0.27	0.36	0.23	0.54	0.24	0.30	0.18	0.40	0.40
CaO	2.85	1.94	2.83	2.79	2.85	2.79	2.99	2.57	2.60
K2O	2.52	2.30	2.25	2.06	2.69	2.13	2.84	2.09	2.13
S	**5.92**	**4.24**	**6.22**	**1.93**	**6.37**	**4.21**	**7.32**	**4.14**	**4.87**
Mn	0.35	0.15	**0.36**	0.27	0.23	0.25	0.23	0.15	0.23

Table 2 Annealing loss of graphite (non-mag fraction) after the first and second flotation, processing of graphite suspension before flotation US (20 kHz, 45°C) for 5, 15 and 30 minutes.

Graphite	Non-mag after 1st flotation	Flotation concentrate non-mag after 2nd flotation	Flotation concentrace non-mag after 5 min US after 2nd flotation	Flotation concentrace non-mag after 15 min US after 2nd flotation	Flotation concentrace non-mag after 30 min US after 2nd flotation
Annealing loss (%)	**38,5**	**64,9**	**69,0**	**81,8**	**89,5**

4 Discussion

The Table 2. shows that the application of the delamination process using US increased the effect of the flotation. Therefore, the amount of combustible carbon (annealing loss) increased after flotation based on time of US application from 64.9 wt.% to 89.5 wt.%, in total of about 25 %. However, the increasement of content of combustible carbon is at the expense of the graphite flakes size. The higher intensity of US leads to flakes crushing (Fig. 5 c, d). The similar results obtained Łoś et al. (2013) and Guittonneau (2010).

The delamination based on triple repeated frost cycles was performed at -18ºC and +24ºC. Delamination based on repeated heating up to 150ºC was conducted at two cycles. The most effective method of delamination of graphite-mica composite was the crushing using US, when the content of combustible particles increased from original 40% (in the concentrate after first flotation) to 95% after second flotation (Fig. 5).

The processing methods were applied for the first time on graphite from Czech Republic.

5 Conclusions

Reserves of graphite ores in the Czech Republic are substantial and reach up to about three millions of tons. The possibility of renewal of graphite mining in the territory of the Czech Republic is dependent on new technologies applied for graphite processing.

Graphite ores available in the Czech Republic contain relatively high amounts of inorganic admixtures predominantly quartz, micas and pyrite and therefore these have to be separated during the ore processing. The sufficient improvement of ore processing has been shown by applying the method of delamination of graphite-mica composite after the second flotation.

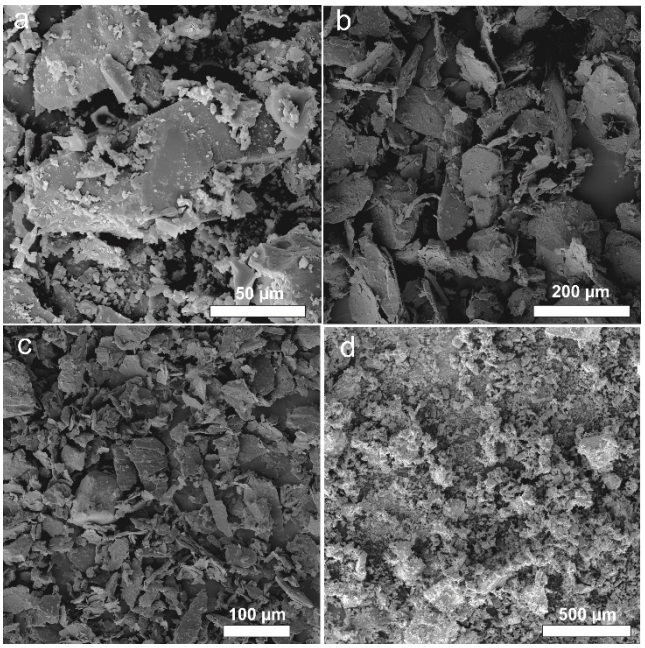

Figure 5. (a) Graphite before processing. (b) Graphite flakes from Lazec deposit. (c) Graphite after floatation before delamination. (d) Delaminated graphite. SEM images.

Acknowledgements

Financial support through the project „Competence Centre for Effective and Ecological Mining of Mineral Resources “(CEEMIR) from the Technology Agency of the Czech Republic (TA ČR), TE 02000029 is gratefully acknowledged.

References

Franěk J, Schulmann K, Lexa O, Tomek Č, Edel J (2011) Model of syn-convergent extrusion of orogenic lower crust in the core of the Variscan belt: implications for exhumation of high-pressure rocks in large hot orogens. J Metamorph Geol 29:53–78.

Guittonneau F, Abdelouas A, Grambow B, Huclier S (2010) The effect of high-power ultrasound on an aqueous suspension of graphite. Ultrason Sonochem 17:391–398.

Jelínek H, Staněk F, Grygar R, Franěk H, Poňavič M (in print) Methodology to 3D modelling of a graphite deposits on the basis of archive data. Geoscience Research Reports 2018.

Łoś S, Duclaux L, Alvarez L, Hawełek Ł, Duber S, Wojciech Kempińsky W (2013) Cleavage and size reduction of graphite crystal using ultrasound radiation. Carbon 55:53–61.

Tichý L (2002) Graphite ores between Cesky Krumlov and Ceské Budejovice. (in Czech) Uhlí-Rudy-Geologický průzkum 9:29–33.

Remediation of cyanide within gold mine waste: an in-depth review of Prussian blue in aqueous solution

Megan D. Welman-Purchase, Robert N. Hansen
University of the Free State

Abstract. Cyanide (CN^-) is used for gold extraction in mining, which creates a potential for dangerous environmental contamination. This research delves into the complexity of the ferro/ferri-cyanide complexes (such as Prussian and Turnbull's blue crystals) and their potential to be a resolution to this contamination. The Fe-CN bond of these complexes are believed to be stable and with the exact combination of bondings may create an inert substance. Although it has been mentioned that pH and redox conditions may affect this stability. This study involves the growth of Prussian and Turnbull's blue single crystals, the analysis of them using single crystal X-ray Diffraction, the affect that strong acids and UV-radiation will have on the stability of the crystals changing the following variables: light intensity, total dissolved salts, pH, temperature, solubility and cyanide complex concentrations. Resulting in the presentation of the best ferro/ferri-cyanide complex for the prevention of CN^- environmental contamination.

1 Introduction

Cyanide in the form of HCN is one of the most toxic chemicals known (Luque-Almagro et al. 2016). There are several industries; including metal plating, mining, synthetic rubber production, pharmaceutical, steel hardening, production of nitrile and nylon, photographic applications and gas production that either use or produce cyanide (Zagury et al. 2004; Akcil 2003). In the mining industry, cyanide is commonly used in the extraction of Ag and Au due to its' high affinity for these elements (Zagury et al., 2004) resulting in the mining industry using 20% of the world's cyanide production yearly (Luque-Almagro et al. 2011). Thus, the mining industry is responsible for the production and potential release of thousands of tons of waste which, along with cyanide, contains toxic metals such as, Hg, Pb and Cd (Luque-Almagro et al. 2016). The threat that cyanide has on human health and the environment is dependent on the chemical speciation (toxicity of the cyanide and physiochemical behaviour) (Meeussen et al. 1992). Cyanide in the gold mining industry can be classified into four categories: free cyanide (CN^- and HCN), readily soluble cyanide (KCN, NaCN), weak acid dissociable cyanide (CN_{WAD} – reasonably unstable containing Ni, Cu, Cd and Zn) and strong acid dissociable cyanide (CN_{SAD} – dissociate in acidic environments containing Au, Ag, Fe and Co) (Zagury et al., 2004). Free cyanide is the most toxic of these due to its high metabolic inhibition potential (Zagury et al., 2004). Free cyanide is produced during the dissociation and dissolution of cyanide complexes in aqueous solutions (Kuyucak and Akcil 2013). At a pH below ~8.5, HCN is produced thus being the main volatilization conditions for free cyanide (Kuyucak and Akcil 2013). For optimum gold extraction, the pH needs to be 10.5 or greater causing the cyanide to form CN^- (Kuyucak and Akcil 2013). The high pH conditions minimise the volatilization of the cyanide (Kuyucak and Akcil 2013).

Soluble cyanide complexes include: NaCN, KCN and $Ca(CN)_2$, which dissipate completely in an aqueous solution (Kuyucak and Akcil 2013). The weakest cyanide complexes (referring to the chemical stability) are Zn and Cd complexes and the strongest complexes are Fe and Co (Kuyucak and Akcil, 2013). Strong acids and UV-radiation may dissociate these complexes releasing free cyanide (Kuyucak and Akcil 2013). Dissociation rate is affected by light intensity, pH, water temperature, complex concentration and TDS (total dissolved salts) (Kuyucak and Akcil, 2013).

According to Meeussen et al. (1992), cyanide is primarily treated and disposed of as iron-cyanide minerals or iron cyanide complexes such as $Fe_4[Fe(CN)_6]_3$. $Fe_4[Fe(CN)_6]_3$ is referred to as Prussian blue and $Fe_3[Fe(CN)_6]_2$ as Turnbull's blue (Weiser et al. 1942), although there is controversy surrounding these terms. The reason for the disposal is the alleged stability of such complexes (Kyle 1997) and the spontaneity of their production (Cosgrove et al. 1972). Other methods of treatment include sulphur dioxide and air process, hydrogen peroxide treatment, alkaline and breakpoint chlorination, biological treatments, among others (Akcil 2003).

Prussian blue can be found in two forms, soluble and insoluble (Adhikamsetty and Jonnalagadda 2009). Insoluble Prussian blue has the chemical formula of $Fe_4[Fe(CN)_6]_3xH_2O$ and soluble Prussian blue has the chemical formula of $KFe[Fe(CN)_6]yH_2O$ (Adhikamsetty and Jonnalagadda 2009). Such minute alterations in the ions incorporated in the crystal structure can lead to the crystals being soluble or insoluble, thus the positioning of the ions in the crystal structure will reveal the solubility of the crystal.

According to the author's knowledge, single crystals of Prussian blue and Turnbell's blue have not yet been grown for the purpose of mining waste remediation. Crystal structures as published in Weiser et al. (1942) and Buser et al. (1977), see figure 1, have been calculated from powder diffraction. Crystals that have been produce are for other purposes such as for material sciences (Nai et al. 2018), for polymer research (Zheng et al. 2007), electrode research (Zadronecki et al. 1999), and so forth, which produce nano-sized crystals. Proving the significance of a crystal structure study, the study of

the positioning of ions in the crystal structure and the other factors that have been mentioned that affect the solubility of the crystals.

The aim of this study is to investigate the stability of the iron-cyanide minerals or iron cyanide complexes. Further studies will involve the implementation of the findings from this study.

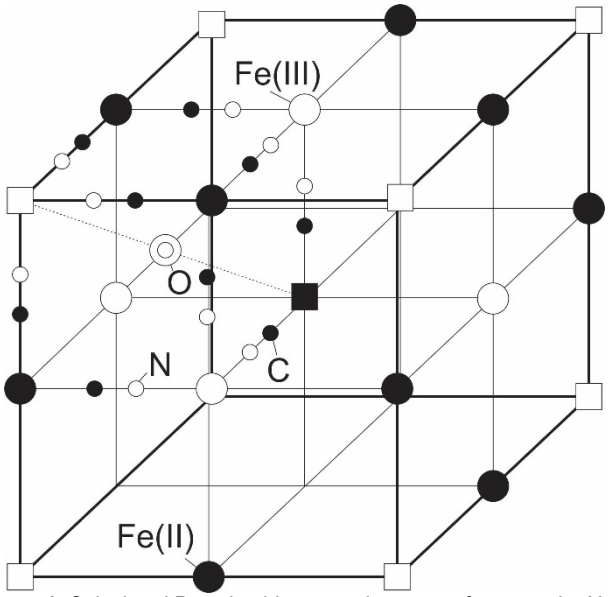

Figure 1. Calculated Prussian blue crystal structure from powder X-ray diffraction, modified after Bruser et al. (1977).

2 Methodology

The first method attempted to produce Prussian blue was by rapidly mixing an aqueous solution of ferric chloride and an aqueous solution of potassium ferrocyanide (Cosgrove et al. 1972). This produces a fine crystalline material, which can be seen in figure 2. The fine material is not sufficient for this study and thus a method of slow diffusion is needed.

The second method currently being attempted involves a single crystal grown using the method mentioned in Buser et al. (1977). A 7.5 mmol solution of $FeCl_2.^3/_4H_2O$ along with 2.5 mmol $K_3[Fe(CN)_6]$ were added to 500 ml 10 mol HCl/L (fig. 2). The solution is then placed in a desiccator containing water, as seen in figure 2. Turnbell's blue crystals are grown using a solution of $FeCl_2$ and $K_3Fe(CN)_6$ (Weiser et al. 1942).

The third method that will be attempted is the crystal growth using the solvent diffusion/growth from gels method as described in Nishinaga (2015). Which involves the slow crystallization where two solutions interact.

3 Final thoughts

Humans are responsible for majority of cyanide environmental contamination. Methods to resolve this issue are of utmost importance. Although the key method of disposal is through ferro/ferri-cyanides, it can be concluded from the literature that there are many factors that influence the stability of these complexes. This proves the significance of an empirical study of these systems.

Figure 2. a. Prussian blue fine-grained crystals produced from rapid mixing of two solutions (potassium ferrocyanide and ferric chloride). **b.** Two solutions used for the single crystal grow. 7.5 mmol solution of $FeCl_2.3/4H_2O$ along with 2.5 mmol $K_3[Fe(CN)_6]$. **c.** The 10 mol of HCl/L solution in a desiccator containing water.

Acknowledgements

Funding for this study is supplied by Iphakade - Earth Stewardship Science.

References

Adhikamsetty RK, Jonnalagadda SB (2009) Kinetics and mechanism of Prussian blue formation. Bull. Chem. Soc. Ethiop. 23(1):47-54

Akcil A (2003) Destruction of cyanide in gold mill effluents: biological versus chemical treatments. Biotechnology Advances 21: 501-511

Buser HJ, Schwarzenbach D, Petter W, Ludi A (1977) The crystal structure of Prussian blue: $Fe_4[Fe(CN)_6)_3.xH_2O$. Inorganic Chemistry, 16, 11, 2704-2710

Cosgrove JG, Collins RL, Murty DS (1972) Preparation of ferrous ferricyanide. Journal of the American Chemical Society, 95, 4, 1083-1086

Kuyucak N, Akcil A (2013) Cyanide and removal option from effluents in gold mining and metallurgical processes. Mineral Engineering 50:13-29

Kyle JH (1997) Stability of metal-cyanide and hydroxide complexes. World Gold '97 Conference. 163-169

Luque-Almagro VM, Blasco R, Martinez-Luque M, Moreno-Vivian C,

Castillo F, Poldan MD (2011) Bacterial cyanide degradation is under review: Pseudoalcaligenes CECT5344, a case of an alkaliphilic cyano troph. Biochem. Soc. Trans. 39:269-274.
Luque-Almagro VM, Moreno-Vivian C, Roldan MD (2016) Biodegradation of cyanide wastes from mining and jewelry industries. Elsevier. 38:9-13
Meeussen JCL, Keizer MK, de Haan FAM (1992) Chemical stability and decomposition rate of iron cyanide in soil solutions. Environ. Sci. Technol. 26:511-516
Nai J, Zhang J, Lou X (2018) Construction of single-crystalline Prussian blue analog hollow nanostructures with tailoable topologies. Chem. 4:1967-1982
Nishinaga T (2015) Handbook of crystal growth, Volume 1 Part B. Elsevier. Amsterdam Netherlands
Weiser HB, Milligan WO, Bates JB (1942) X-ray diffraction studies on heavy-metal iron-cyanides. J. Phys. Chem. 46(1):99-111
Zagury GJ, Oudjehani K, Deschênes L (2004) Characterization and availability of cyanide in solid mine tailings from gold extraction plants. Sci. Total. Eviron. 320:211-224
Zadronecki M, Wrona PK, Galus Z (1999) Study of growth and the electrochemical behavior of Prussian blue films using electrochemical quartz crystal microbalance. ElectroChem. Soc. 146(2):620-627
Zheng XJ, Kuang Q, Xu Tao, Jiang ZY, Zheng SH, Xie ZX, Huang RB, Zheng LS (2007) Growth of Prussian blue microcubes under a hydrothermal condition: possible nonclassical crystallization by a mesoscale self-assembly. J.Phys. Chem, 111:4499-4502

Fungal extraction of Se and Te from the Kisgruva Proterozoic volcanogenic massive sulfide deposit

Xinjin Liang[1], Magali A.M. Perez[2], Joseph G. Armstrong[2], Liam A. Bullock[2], Jorg Feldmann[2], Laszlo Csetenyi[1], Geoffrey M. Gadd[1]
[1]*University of Dundee, Scotland, UK*
[2]*University of Aberdeen, Scotland, UK*

Abstract. Microbial Se or Te reduction offers a potential route to biorecovery of these elements. Reduction is often efficient and large amounts of these metalloids can be removed from solution because of extensive precipitation of elemental forms. In this research, *Aureobasidium pullulans, Mortierella humilis, Trichoderma harzianum*, *Phanerochaete chrysosporium*, *Phoma sp.,* and *Phoma glomerata* were used to investigate their potential to extract Se and Te from selenium and tellurium resources in the Kisgruva Proterozoic volcanogenic massive sulfide deposit. All microorganisms were able to grow in selenium- and tellurium-containing sulfide ore liquid media and extract these elements from the ores. The findings are relevant to novel approaches for selenium and tellurium biorecovery from liquid and rock matrices as well as bioremediation.

1 Introduction

Many microorganisms are capable of transforming various selenium and tellurium species through methylation, oxidation, reduction and demethylation (Jacob et al. 2016; Eswayah et al. 2016). Filamentous fungi are capable of extracellular and intracellular synthesis of selenium particles making processing and biomass handling easier and hence perhaps more preferable than unicellular organisms (Mandal et al. 2006). The large amounts of extracellular produced enzymes and reductive proteins make fungi an unique investigation system (Gharieb et al. 1999; Gharieb and Gadd 2004; Espinosa-ortiz et al. 2017). Filamentous fungi like *Trichoderma harzianum* have been reportedly used for the extracellular biomass-free synthesis of silver nanoparticles. *T. harzianum* has been used as a biological control agent because of its multi-enzymatic system composed of chitinases, β-glucanases and proteases (Siddiquee et al. 2014). Several naphthoquinone and anthraquinone compounds from *T. harzianum* possess good reducing properties (Siddiquee et al. 2014). *Pseudomonas sp.* (Hunter and Manter 2009), *Alternaria alternata* (Sarkar et al. 2012), and *Phanerochaete chrysosporium* (Espinosa-Ortiz et al. 2015) were able to generate selenium nanoparticles from reduction of either selenate or selenite, while *Fusarium sp., Penicillium citrinum* (Gharieb et al. 1999), *Saccharomyces cerevisiae* (Gharieb and Gadd 2004), and *Rhodotorula mucilaginosa* (Ollivier et al. 2011) can produce nanoscale elemental Te from tellurite. *P. chrysosporium* also produced mixed Se-Te nanoparticles when grown with selenite/tellurite (Espinosa-Ortiz et al. 2017). The application of microbial Se or Te reduction offers a potential route for biorecovery of these elements from solution and solid substrates.

This research explored the potential of selected fungal strains as selenium- and/or tellurite-reducing organisms and their potential to extract Se and Te elements from selenium and tellurium resources in the Kisgruva Proterozoic volcanogenic massive sulfide deposit. The objectives were to determine: (1) the effect of sulfide ores on fungal growth and morphology modification, (2) the different composition of sulfide ores before and after fungal growth, (3) Se and Te extraction rates after growth with selected fungi.

2 Sequential extraction and metalloid speciation in the Kisgruva sulfide ores

Sequential extraction and speciation were performed on Kisgruva sulfide ore samples 450, 456 and 459 to determine the total amounts of Se and Te associated with oxide minerals and organic matter (Bullock et al. 2018). Concentrations of selenium and tellurium species adsorbed to charged surfaces, such as oxide minerals, were determined using a phosphate buffer extraction method (Fig. 1 blue), while concentrations and speciation of selenium and tellurium bound to organic matter were examined by a sodium hydroxide extraction method (Fig. 1 orange). The Aqua regia residues method was used for total extractable concentrations of selenium and tellurium (Fig. 1 grey). Both selenite (SeO_3^{2-}) and tellurite (TeO_3^{2-}) were identified in sulfide ore crust samples by phosphate and sodium hydroxide extraction methods (Fig. 1), but elemental forms (Se^0 and Te^0) or selenate (SeO_4^{2-}) / tellurate (TeO_4^{2-}) were not detected. For sample 450, of the extractable Se (14.3% of total Se), only 39.5% was associated with oxide minerals, with 60.5% bound to organic matter (Se(-II)). For extracted Te (31.4%), 22% was associated with oxide minerals, and 78% with organic matter. Similar results were observed for sample 459, with total extractable Se, associated with oxide minerals and bound to organic matter of 27%, 20.9% and 79.1% respectively. For Te, the percentages were 24.2%, 20.9% and 79.1% respectively. More selenium was bound to organic matter in sample 456, compared to the other samples, with total extractable Se, associated with oxide minerals and bound to organic matter of 74.2%, 7% and 93% respectively. For Te, the respective percentages were 10.9%, 15.4% and 84.6%.

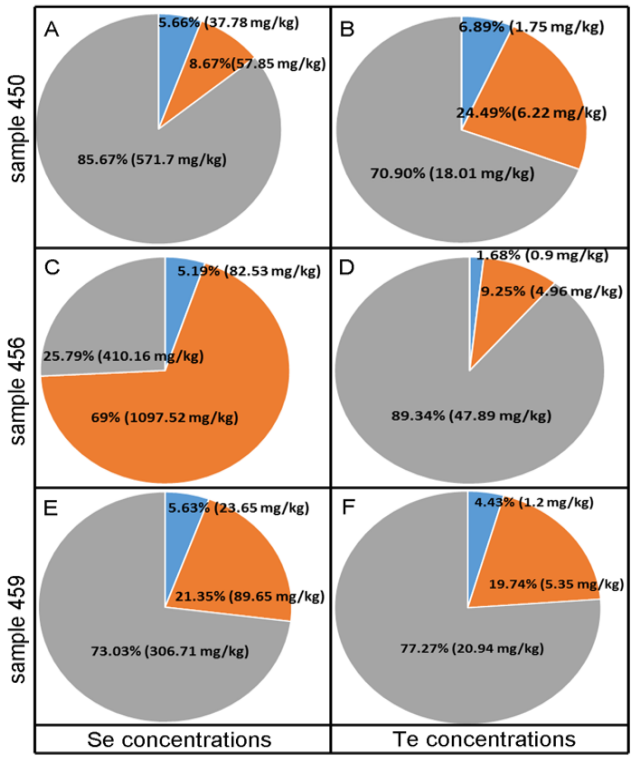

Figure 1. Se and Te speciation revealed by extraction with phosphate buffer (blue), sodium hydroxide (orange) and Aqua regia (grey) extraction methods for samples 450, 456 and 459. All values shown are means of at least three measurements with typical relative standard deviations of about 5%.

3 Tolerance indices of selected fungi grown with Kisgruva sulfide ores

Tolerance indices (TI) were used to compare fungal biomass yields grown in AP1 medium with or without sulfide ore samples (Fig. 2). A TI value lower than 100 indicates growth inhibition, whereas larger than 100 suggests growth stimulation. The tolerance indices for sulfide ore samples varied between different fungal strains. In the presence of samples 450, 456 and 459, all fungi showed growth reduction. For sample 450, growth of *P. chrysosporium, T. harzianum* and *Phoma. sp* was significantly ($P < 0.05$) inhibited by 43%, 19% and 51% respectively, while *A. pullulans, M. humilis* and *P. glomerata* showed relatively better tolerance (Fig. 2). In the presence of sample 456, *T. harzianum* showed the most inhibition (34%). There were no significant inhibitory effects on *P. chrysosporium,* and *Phoma. sp* in the presence of sample 459, while biomass yields were markedly reduced for *A. pullulans* and *M. humilis* (Fig. 2).

All fungi were able to grow in the presence of sulfide ore samples 450, 456 and 459 after 30 days incubation at 25°C. The original media pH values for samples 450, 456 and 459 were 3.9, 2.2 and 7.9 respectively. There were no significant differences in the media pH values on addition of samples 450 and 456. Compared to the controls grown in ore-free AP1 medium, growth of the fungal strains lowered the pH values from 3.9 to between 1.8 to 2.9 for sample 450, and from 2.2 to between 1.9 to 3 for sample 456. The pH values for sample 459 in the presence of the fungi increased slightly after 30 days incubation except for *P. chrysosporium* and *Phoma. sp* (Fig. 2).

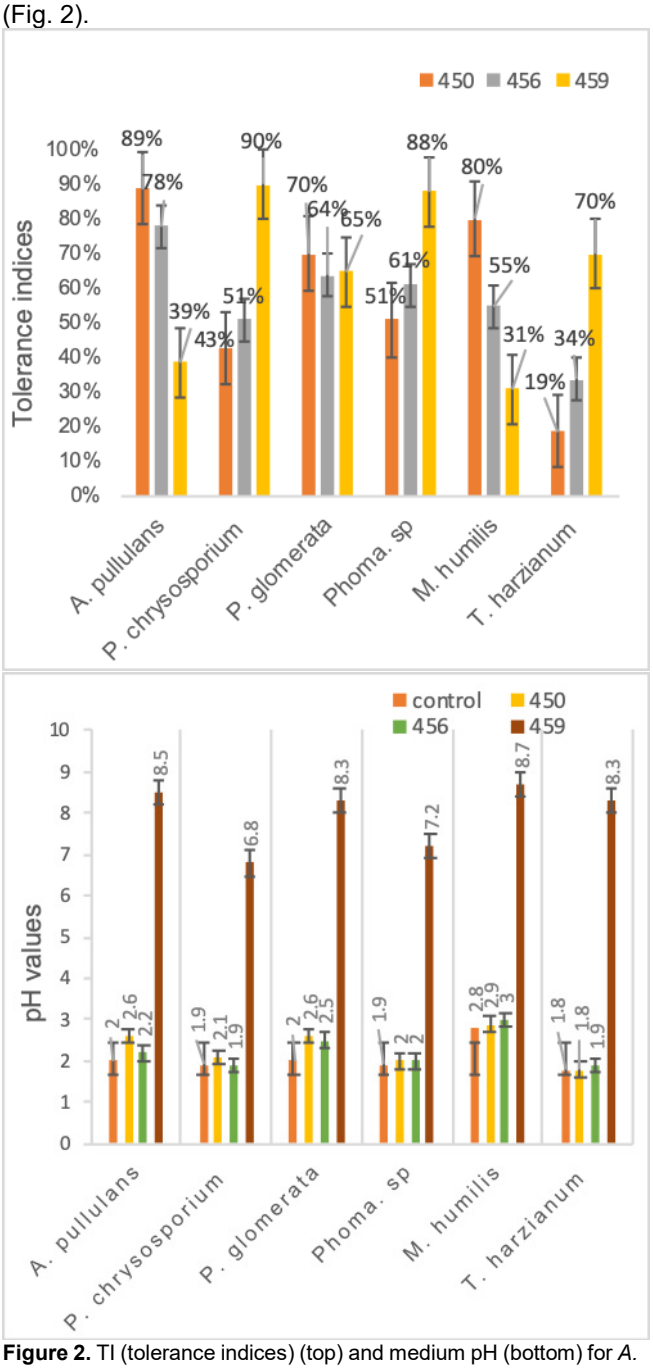

Figure 2. TI (tolerance indices) (top) and medium pH (bottom) for *A. pullulans, P. chrysosporium, M. humilis, T. harzianum, Phoma. sp.* and *P. glomerata* grown in AP1 medium amended with samples 450, 456 and 459. All values shown are means of at least three measurements with typical relative standard deviations of about 5%.

4 Composition of the Kisgruva sulfide ores before and after fungal growth

The sulfide ore at the Kisgruva mine site was originally used for extraction of copper, sulfur and iron, but also contains high concentrations of selenium and tellurium. Elements present in the sulfide ore samples were determined by X-ray fluorescence (XRF) before and after

growth with fungi for 30 days. Both Se and Te were also present within the sulfide ores in pyrite and chalcopyrite (sample 450 and sample 459), which contained high concentrations of up to 688 ppm Se and 81 ppm Te (Bullock et al., 2018), together with the major and trace elements, including Fe, S, P, Al, Ca, K, Fe, Mg, Si, Ti, Co, Na, Ni, Cu, Zn, Cl, Pb, W and As. There were no significant differences observed with the composition of sulfide ore samples 450, 456 and 459 before and after fungal growth (Fig. 3, data for samples 456 and 459 not shown). The presence of fungi helped to leach most of the elements from the sulfide ore, however, only small proportional changes were observed for certain elements (Fig. 3). Since the XRF analysis assumes the sample matrix all in oxidic condition, the real compositions of the sulfide ore samples were too complicated to conclude by XRF on its own, it only gives oxidic composition percentages for elements detected, the further laser ablation analysis should give detailed element changes.

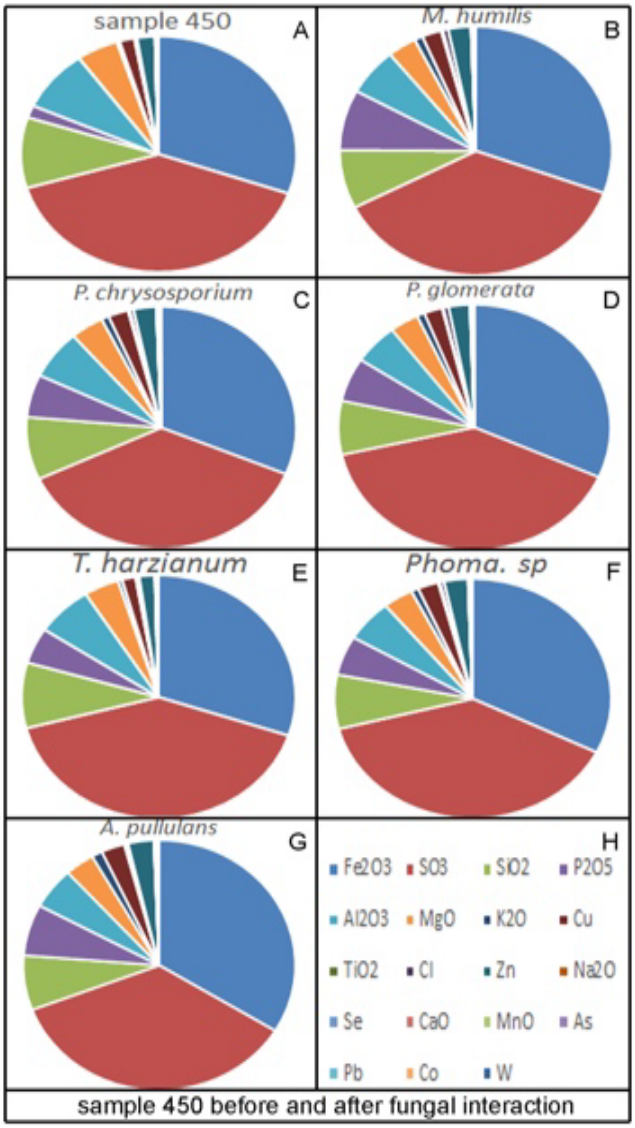

Figure 3. Elemental composition of sulfide ore sample 450 before and after fungal growth. Kisgruva sulfide ore sample was incubated with selected fungi in AP1 liquid media for 30 days at 25°C in the dark at 125 rpm. All values shown are means of at least three measurements with typical relative standard deviations of about 5%.

5 Fungal extraction of selenium and tellurium from Kisgruva sulfide ores

P. glomerata was chosen for further experiments, because of good tolerance of the sulfide ores. *P. glomerata* was grown on polished flat surfaces of samples 450 and 459 for 30 days on MEA plates to investigate its ability for selenium and tellurium extraction. Trace element analysis of polished sulfide ore blocks of generally inclusion-free pyrite was performed by using a new wave laser ablation system UP213 nm coupled to an ICP-MS Agilent 7900. Samples 450 and 459 were high in other chalcophile elements which showed a chemical affinity to Se and Te, such as Fe (380041 ppm, 633668 ppm), Cu (476 ppm, 2124 ppm), As (408 ppm, 376 ppm), Ag (26 ppm, 62 ppm), Au (0.2 ppm, 0.2 ppm), Hg (0.7 ppm, 1.4 ppm) Pb (1274 ppm, 189 ppm) and Bi (17 ppm, 30 ppm) respectively. Sulfide ore samples contained an average of 0.05% TOC (Fig. 4). All elements in the sulfide ore samples showed marked removal after growth with *P. glomerata*. Selenium and tellurium from sulfide ore samples 450 and 459 were extracted by *P. glomerata* with removals of 66-77% for selenium and 72% for tellurium confirmed by the laser ablation (LA) ICP-MS analysis (Fig. 4). Laser ablation analysis showed that Se, and Te to a lesser extent were present, even though Te was generally high throughout the pyrite phases (Bullock et al. 2018). For As, Se and Te, concentrations were higher towards the edges of the pyrite for samples 450 and 459. As well as a high content throughout pyrite, Se and Te also showed disseminated areas of high concentration, in some instances, up to 10,000 ppm and 1000 ppm respectively. Though the selected pyrite crystals were generally inclusion-free, these Se and Te hotspots may correspond to micron-sized Se^{2-} and Te^{2-} (Bullock et al. 2018). After growth with *P. glomerata*, Se and Te hotspot concentrations for sample 450 dropped down to 1000 ppm and 100 ppm respectively, while for sample 459, concentrations dropped down to 100 ppm on both selenium and tellurium (Fig. 4).

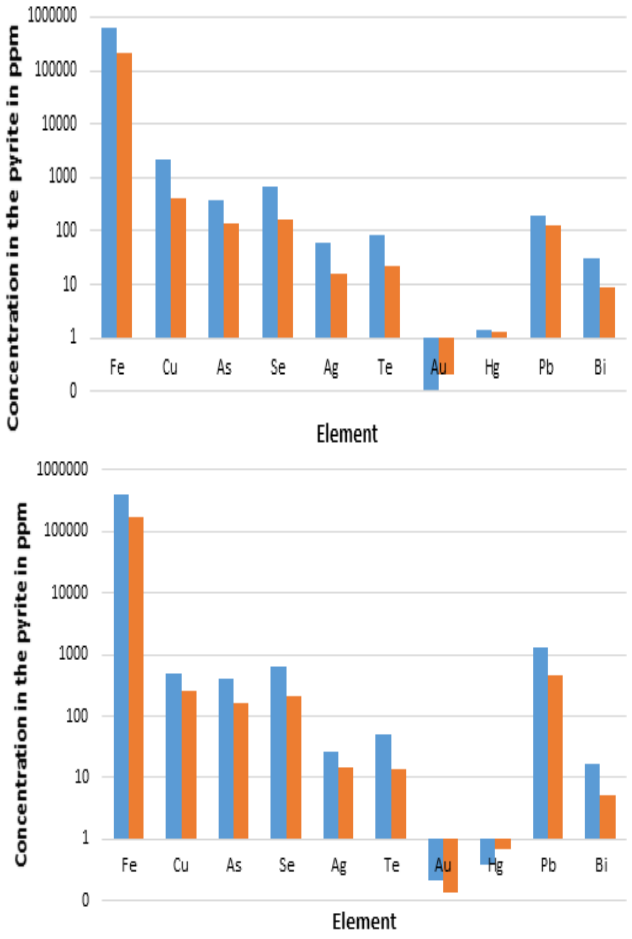

Figure 4. Concentrations of all elements in the sulfide ore samples 450 (top) and 459 (bottom) before (blue) and after (orange) growth with *P. glomerata* for 30 days at 25°C in the dark. Typical results are shown from one of at least three determinations.

6 Implications

Bioremediation and biorecovery of Se and Te from selenium- and tellurium-polluted environments suggest an environmentally-sustainable choice of treatment for contaminated soils, groundwater, wastewater and sediments (Liang and Gadd 2017). The potential application of bioextraction of Se and Te may be developed through established protocols and optimized processes. Previous research has demonstrated Se- or Te-species removal by fungi is accomplished through intracellular uptake or interaction with surface biomolecules such as proteins, amino acids and extracellular polymeric substances, while cellular biotransformation of selenium and tellurium oxyanions leads to reduction to elemental selenium and tellurium. Both elemental selenium and tellurium were found within the fungal biomass and in supernatants. A challenge in the biogenic production of selenium and tellurium nanoparticles is their purification from fungal biomass, because the formation of selenium and tellurium nanoparticles can be achieved both intracellularly and extracellularly: separation of particles from biomass without altering their properties, shape and size is challenging (Liang et al. 2019). These findings from the fungal interaction with sulfide ore samples are relevant to novel approaches for biorecovery of these elements as elemental selenium and tellurium by the fungal surface biomolecules straight from the ore samples.

Acknowledgements

G. M. Gadd gratefully acknowledges research support from the Natural Environment Research Council [NE/M010910/1 (TeaSe); NE/M011275/1 (COG3)]. The authors also gratefully acknowledge the help of Dr Yongchang Fan (Materials and Photonics Systems Group, University of Dundee, Dundee, DD1 5EH, Scotland UK) for assistance with scanning electron microscopy.

References

Bullock LA, Perez M, Armstrong JG, Parnell J, Still J, Feldmann J (2018) Selenium and tellurium resources in Kisgruva Proterozoic volcanogenic massive sulfide deposit (Norway). Ore Geol Rev 99:411-424.

Espinosa-ortiz EJ, Gonzalez-Gil G, Saikaly PE, van Hullebusch ED, Lens PNL (2015) Effects of selenium oxyanions on the white-rot fungus *Phanerochaete chrysosporium*. Appl Microb Biotechnol 99:2405-2418.

Espinosa-ortiz EJ, Rene ER, Guyot F, van Hullebusch ED, Lens PNL (2017) Biomineralization of tellurium and selenium-tellurium nanoparticles by the white-rot fungus *Phanerochaete chrysosporium*. Int Biodeterior Biodegradation 124:258-266.

Eswayah AS, Smith TJ, Gardiner PH (2016) Microbial transformations of selenium species of relevance to bioremediation. Appl Environ Microbiol 82:4848-4859

Gharieb MM, Gadd GM (2004) Role of glutathione in detoxification of metal(loid)s by *Saccharomyces cerevisiae*. BioMetals 17:183-188.

Gharieb MM, Kierans M, Gadd GM (1999) Transformation and tolerance of tellurite by filamentous fungi: accumulation, reduction, and volatilization. Mycol Res 103: 299-305.

Hunter WJ, Manter DK (2009) Reduction of selenite to elemental red selenium by *Pseudomonas sp.* strain CA5. Curr Microbiol 58:493-498.

Jacob JM, Lens PNL, Balakrishnan RM (2016) Microbial synthesis of chalcogenide semiconductor nanoparticles: a review. Microb Biotechnol 9:11-21.

Liang X, Gadd GM (2017) Metal and metalloid biorecovery using fungi. Microb Biotechnol 10:1199-1205.

Liang X, Perez MAM, Feldmann J, Csetenyi L, Gadd GM (2019) Formation of selenium- and tellurium-containing nanoparticles during the growth of filamentous fungi. Acce Microbiol (doi: 10.1099/acmi.ac2019.po0286).

Mandal D, Bolander ME, Mukhopadhyay D, Sarkar G, Mukherjee P (2006) The use of microorganisms for the formation of metal nanoparticles and their application. Appl Microb Biotechnol 69:485-492.

Ollivier PRL, Bahrou A, Church TM, Hanson TE (2011) Aeration controls the reduction and methylation of tellurium by the aerobic, tellurite-resistant marine yeast *Rhodotorula mucilaginosa*. Appl Environ Microbiol 77: 4610-4617.

Sarkar J, Saha S, Dey P, Acharya K (2012) Production of selenium nanorods by phytopathogen, *Alternaria alternata*. Adv Sci Lett 10:111-114.

Siddiquee S, Rovina K, Yusof NA, Rodrigues KF, Suryani S (2014) Nanoparticle-enhanced electrochemical biosensor with DNA immobilization and hybridization of *Trichoderma harzianum* gene. Sens Biosensing Res 2:16-22.